Mathematics

AIMS Mathematics, 11(1): 127–166.
DOI: 10.3934/math.2026006
Received: 08 October 2025
Revised: 30 November 2025
Accepted: 09 December 2025
Published: 04 January 2026

https://www.aimspress.com/journal/Math

---

***Research article***

# Application of fractional derivatives in the Guyer and Krumhansl heat transfer control model for magneto-thermoelastic analysis of transversely isotropic annular cylinders

**Mofareh Alhazmi[1,*], Ahmed E. Abouelregal[1,*] and Marin Marin[2,3]**

[1] Department of Mathematics, College of Science, Jouf University, Sakaka 77455, Saudi Arabia
[2] Department of Mathematics and Computer Science, Transilvania University of Brasov, Brasov, Romania
[3] Academy of Romanian Scientists, Bucharest, Romania

* **Correspondence:** Email: mmmhazmi@ju.edu.sa, ahabogal@ju.edu.sa; Tel: +966551386829.

**Abstract:** In this study, we presented a novel fractional nonlocal thermoelastic heat conduction model that extends the Guyer–Krumhansl framework by incorporating size-dependent nonlocal thermal effects and non-Fourier heat conduction characteristics. The model extends the traditional approach using the single-phase-lag (SPL) method derived from Moore–Gibson–Thompson (MGT) heat theory. By employing the Atangana–Baleanu (AB) fractional derivative with a non-singular kernel, we integrated nonlocal features through fractional derivatives, enhancing its applicability to complex thermal behaviors in materials exhibiting combined nonlocal and fractional dynamics. To validate the model, thermoelastic interactions were examined in a long, hollow cylinder subjected to a uniform electromagnetic field. The outer surface was thermally insulated and traction-free, while the inner surface, also traction-free, experienced thermal shock. Governing equations were solved using the Laplace transform method, and numerical solutions were obtained via the Dubner–Abate algorithm. The results were compared with conventional and generalized thermoelastic models to assess accuracy and effectiveness. Additional analysis explored material properties through graphical data, considering various fractional orders and operators, thereby enriching the understanding of system behavior under different conditions. The findings demonstrated the advantages of the fractional nonlocal thermoelastic model in capturing complex thermal interactions within advanced materials, contributing significantly to heat conduction theory.

**Keywords:** MGT thermoelasticity; fractional-order; transversely medium; Atangana–Baleanu fractional derivative; Mittag–Leffler
**Mathematics Subject Classification:** 65M38, 78M15, 80M15

## Nomenclature

| Symbol | Description |
|---|---|
| $\vec{q}$ | Heat flow vector |
| $K$ | Thermal conductivity |
| $\theta = T - T_0$ | Temperature change (difference between absolute and reference temperatures) |
| $T$ | Absolute temperature |
| $T_0$ | Reference temperature |
| $\tau_0$ | Relaxation time |
| $\vec{P}$ | Position (location) vector |
| $K^*$ | Thermal conductivity rate |
| $\psi$ | Thermal displacement function |
| $C_E$ | Specific heat at constant strain |
| $Q$ | Heat source |
| $\rho$ | Material density |
| $t$ | Time variable |
| $\beta_{ij} = c_{ijkl}\alpha_{kl}$ | Thermal coupling parameters |
| $\alpha_{kl}$ | Coefficients of linear thermal expansion |
| $c_{ijkl}$ | Elastic stiffness coefficients (fourth-order elastic tensor) |
| $\sigma_{ij}$ | Stress tensor |
| $e_{ij}$ | Strain tensor |
| $u_i$ | Components of the displacement vector |
| $\vec{J}$ | Conduction current density |
| $\vec{E}$ | Electric field intensity |
| $\vec{h}$ | Induced magnetic field vector |
| $\vec{B}$ | Magnetic flux density |
| $\vec{D}$ | Electric flux density |
| $\mu_0$ | Magnetic permeability (of free space) |
| $\varepsilon_0$ | Electric permittivity (of free space) |
| $F_i$ | Components of the Lorentz force |
| $\sigma_0$ | Electrical conductivity |

## 1. Introduction

The theoretical and experimental investigation of coupled thermal and mechanical responses in solids has long been a cornerstone of continuum mechanics. Classical thermoelasticity, rooted in Fourier's law of heat conduction and Biot's linear coupling framework, has provided foundational insights into how temperature gradients induce stress and deformation in elastic media [1]. However, as engineering systems increasingly operate under extreme thermal transients, high-frequency excitations, or at micro- and nanoscales, the limitations of classical models become evident. Most notably, the parabolic nature of Fourier-based heat equations implies an infinite propagation speed for thermal signals, a physical impossibility contradicted by experimental evidence and relativistic causality [2]. This discrepancy has spurred the development of generalized thermoelastic theories that incorporate finite thermal wave speeds and account for microstructural and memory-dependent effects [3].

Despite their historical significance, classical theories of heat conduction, exemplified by Fourier's law, suffer from inherent paradoxes that limit their applicability in certain scenarios. The most prominent issue is the prediction of infinite heat propagation speed, which contradicts the principles of relativity and experimental observations of finite thermal wave speeds in materials [4]. This "paradox of infinite speed" becomes particularly problematic in transient heat transfer processes, such as those involving ultrashort laser pulses or cryogenic applications, where thermal waves exhibit wave-like characteristics rather than purely diffusive behavior. Biot's coupled thermoelasticity [5], while advancing the field by incorporating mechanical effects into thermal equations, inherits this limitation through its parabolic heat equation.

To overcome the limitations of Fourier-based approaches, researchers have developed non-Fourier models that account for finite heat propagation speeds. The Cattaneo–Vernotte (CV) model [6], for example, introduces a relaxation time that transforms the heat equation from parabolic to hyperbolic, enabling thermal wave propagation. This concept was further generalized by Lord and Shulman [7], who incorporated Maxwell's ideas into thermoelasticity, establishing a framework in which both heat and elastic waves propagate at finite velocities. Building on this foundation, Green and Naghdi [8–10] proposed three types of thermoelastic theories (GN-I, GN-II, GN-III), with GN-III being particularly versatile as it includes both dissipative and non-dissipative terms, allowing the modeling of undamped thermal waves.

Moreover, the MGT equation has emerged as a sophisticated extension derived from acoustic wave principles and adapted to thermoelasticity [11,12]. By introducing higher-order time derivatives and relaxation parameters, the MGT model resolves instabilities present in earlier formulations and provides a stable description of thermal processes in damped systems [13]. These advancements have proven crucial in applications involving rapid thermal transients, such as semiconductor devices and shock-wave lithotripsy, where precise control of heat dissipation is essential [14]. Furthermore, the incorporation of electromagnetic effects through Maxwell's equations and Ohm's law enriches these models, enabling the analysis of magneto-thermoelastic coupling in conductive materials [15,16].

In contemporary contexts, thermoelastic phenomena are not merely academic; they underpin the reliability and safety of advanced structures. For example, in aerospace engineering, thermal expansion and contraction of components during atmospheric re-entry can lead to catastrophic failures if not accurately predicted [17]. Similarly, in biomedical applications such as prosthetic implants, understanding thermoelastic responses is essential for ensuring biocompatibility and long-term performance. The integration of magnetic fields adds another layer of complexity, as seen in magneto-thermoelasticity, where electromagnetic interactions influence thermal and mechanical properties. This multidisciplinary nature has driven researchers to move beyond isotropic assumptions, focusing on anisotropic materials such as transversely isotropic composites, which exhibit direction-dependent properties common in layered structures [18]. As researchers delve deeper into these interactions, it becomes evident that a holistic approach is necessary to capture the full spectrum of behaviors in modern materials.

Fractional calculus, with its ability to model memory-dependent and hereditary phenomena, has revolutionized the analysis of complex systems where integer-order derivatives fall short [19]. Unlike classical calculus, which assumes local and instantaneous interactions, fractional derivatives capture long-range dependencies and anomalous diffusion, making them ideal for materials with fractal microstructures or viscoelastic properties [20,21]. The Riemann–Liouville and Caputo definitions laid the foundation, but their singular kernels limited applicability in certain cases [22]. Moreover, the Atangana–Baleanu (AB) fractional derivative [23,24], featuring a non-singular Mittag–Leffler kernel, addresses these limitations by providing a more physically consistent representation of memory effects without mathematical singularities.

In heat transfer, fractional models extend non-Fourier theories by introducing fractional orders into relaxation times or heat flux equations, enabling the simulation of sub- and super-diffusive behaviors observed in heterogeneous media [25]. For example, in biological tissues and porous materials [26,27], heat transfer often deviates from classical diffusion due to irregular pathways, and fractional calculus effectively quantifies these anomalies. Studies have shown that AB-based models outperform traditional fractional approaches in predicting thermal responses under varying loads, offering smoother transitions and better agreement with experimental data. This integration not only enhances predictive accuracy but also facilitates the optimization of thermal management in advanced composites [28].

Nonlocality in heat conduction recognizes that thermal responses at a point depend on the temperature field over a finite region rather than solely on local conditions. This concept is particularly relevant in nanomaterials, where the mean free paths of heat carriers exceed structural dimensions, leading to ballistic transport [29]. The Guyer–Krumhansl (GK) model [30] exemplifies this approach by augmenting the Cattaneo–Vernotte equation with a nonlocal length-scale parameter, thereby accounting for spatial dispersion and size effects. Derived from phonon hydrodynamics, the GK framework introduces terms related to heat flux curvature, effectively capturing phenomena such as Knudsen layers in thin films [31,32].

Combining nonlocal effects with fractional derivatives yields hybrid models that address temporal memory and spatial nonlocality, providing a comprehensive framework for analyzing complex thermal behaviors [33]. In transversely isotropic materials, where properties vary directionally, these models are indispensable for accurately predicting anisotropic heat flow [34]. Applications extend to microelectronics, where nonlocal effects help mitigate hotspots, and to energy-harvesting devices, where efficient heat-to-work conversion relies on precise modeling of thermal gradients [35].

Magneto-thermoelasticity explores the synergistic effects of magnetic fields on thermoelastic systems by incorporating Lorentz forces and Joule heating. In conductive materials exposed to magnetic fields, induced currents modify stress distributions, potentially enhancing or damping thermal expansion [36]. For infinitely long annular cylinders, common in pipelines, pressure vessels, and rotating machinery, this coupling becomes critical, as radial symmetries amplify electromagnetic influences [37]. Transversely isotropic cylinders, often employed in composite rotors or magnetic bearings, exhibit unique responses due to fiber orientations, necessitating specialized analyses. The presence of a uniform magnetic field along the axial direction induces secondary electric and magnetic fields governed by Maxwell's equations, which interact with thermal waves. This configuration provides an ideal framework for studying phenomena such as magnetocaloric effects and electromagnetic damping in vibrational systems [38]. Numerical techniques, such as Laplace transforms, facilitate solving these coupled equations, offering insights into wave attenuation and stress concentration patterns.

Said's research advances generalized thermoelasticity by integrating nonlocality, memory, and multiphysics effects. Studies include: a 2D nonlocal rotating half-space with memory-dependent derivatives [39]; phase-lag, rotation, and temperature-dependent wave propagation in a magneto-microstretch medium [40]; a thermo-magneto-viscoelastic model with variable conductivity under gravity [41]; and a two-temperature magneto-thermoelastic model with dual-phase-lag, gravity, and initial stress [42]. Collaborations with Othman extend to electro-magneto-thermoelasticity with two-temperature and internal heating [43] and magnetic-field effects in a nonlocal porous solid with memory-dependent derivatives [44]. This body of work systematically unifies memory-dependent, dual-phase-lag, two-temperature, and magneto-thermo-viscoelastic formulations, providing a robust framework for modeling advanced materials under complex multiphysical loads. Complementing this, recent contributions by Alhasan et al. [45], Mohammad et al. [46], and Körpinar et al. [47] demonstrate the growing role of fractional calculus in fluid dynamics and heat transfer, particularly in boundary-layer flows over permeable cylinders and electroosmotic systems, where fractional derivatives capture memory and non-locality in transport processes. Furthermore, Abro et al. [48] extend these concepts to chaotic convection in porous media by comparing fractal and fractional non-equilibrium thermal models. Together, these studies underscore a paradigm shift toward fractional, nonlocal, and multi-field coupled models that better represent real-world material behavior in advanced engineering, aerospace, biomedical, and energy applications.

In light of evolving demands in engineering and materials science, we address a critical research gap in integrating fractional nonlocal models with magneto-thermoelasticity for annular structures. While researchers have examined fractional derivatives or nonlocal effects independently, few have combined them within the GK framework augmented by MGT equation and AB fractional operators, particularly under magnetic influences. The novelty of this work lies in proposing a generalized fractional nonlocal thermoelastic model that incorporates non-singular kernels, ensuring enhanced stability and accuracy in capturing complex thermal dynamics. Key contributions include the derivation of governing equations that unify temporal fractional delays, spatial nonlocality, and electromagnetic coupling, along with analytical solutions for transversely isotropic cylinders subjected to thermal shocks and magnetic fields.

The proposed model is applied to a hollow annular cylinder with a traction-free inner surface exposed to exponential thermal pulses and an insulated outer surface, illustrating how fractional orders influence wave propagation and stress fields. Using the Laplace transform method with numerical inversion via the Dubner–Abate technique, the study provides insights into system behavior under varying parameters. The key findings reveal that lower fractional orders amplify memory effects, resulting in slower heat dissipation and more pronounced nonlocal influences, while AB derivative offers superior modeling of hereditary properties compared to Caputo alternatives, yielding more realistic predictions of temperature, displacement, and stress distributions.

This framework enhances the design of electromagnetic–thermal devices such as MRI components and fusion reactor liners by enabling better prediction of failure modes and optimization of material performance under extreme conditions, contributing to safer and more efficient engineering solutions. These theoretical advances translate into tangible engineering benefits across multiple high-tech domains. In nuclear fusion systems, the stress-mitigating effect of nonlocality can significantly extend the fatigue life of first-wall components exposed to plasma thermal shocks. In aerospace turbine blades, the phase-lag behavior induced by fractional memory enables more accurate prediction of thermally induced creep, allowing for lighter, more efficient designs. For biomedical metallic implants, the smoother thermal and displacement fields predicted by AB kernel reduce micro-motion at the bone–implant interface, lowering the risk of aseptic loosening during MRI scans. Moreover, in microelectronic thermal management, the model's ability to suppress thermal hotspots via nonlocal dispersion offers a pathway to enhance reliability in high-power RF and quantum devices. These examples underscore the model's readiness for real-world deployment in systems where classical Fourier-based approaches fail.

## 2. Derivation of the mathematical framework

In this section, we present the foundational equations for modeling heat conduction and thermoelastic behavior in homogeneous transversely isotropic materials, incorporating nonlocal and fractional effects. The framework begins with classical thermoelastic relations and evolves toward a generalized fractional model that accounts for temporal memory and spatial dispersion [49]:

$$\sigma_{ij} = c_{ijkl}\varepsilon_{kl} - \beta_{ij}\theta. \tag{1}$$

The strain-displacement relation is defined as [50]:

$$\varepsilon_{ij} = \frac{1}{2}\left(\frac{\partial u_i}{\partial x_j} + \frac{\partial u_j}{\partial x_i}\right). \tag{2}$$

The dynamic equilibrium equation, incorporating body forces $F_i$, is expressed as [51]:

$$c_{ijkl}\varepsilon_{kl,i} + F_i = \rho\frac{\partial^2 u_i}{\partial t^2},\ \ i,j\ =\ 1,2,3. \tag{3}$$

The assumption of instantaneous heat propagation in classical Fourier's law renders it inadequate for modeling high-frequency or nanoscale thermal processes. To resolve this shortcoming, Cattaneo and Vernotte introduced a relaxation time $\tau_0$, which led to a modified heat flux equation [52]:

$$\left(1 + \tau_0\,\frac{\partial}{\partial t}\right)q_i = -K_{ij}\frac{\partial\theta}{\partial x_j}. \tag{4}$$

As research shifts to micro- and nanoscale systems, size-dependent effects become critical for accurate material behavior prediction. Classical continuum theories, assuming locality, homogeneity, and instantaneous interactions, fail at these scales where size-dependent stiffness, stress/strain gradients, and nonlocal interactions dominate, particularly in complex microstructures and nanostructured environments.

Nonlocal phase-lag theories address classical heat transfer limitations by incorporating spatial nonlocality and temporal delays, unlike Fourier's law which assumes instantaneous, local and thermal propagation [53]. These frameworks capture transient behavior and size-dependent effects crucial for nanoscale and ultrafast thermal processes in microelectronics, photothermal therapies, and nanoscale energy systems [29,54]. The Guyer–Krumhansl (GK) [33] and dual-phase-lag (DPL) [55] theories are leading models in this field. The GK model enhances classical heat conduction through two modifications: single-phase-lag parameter $\tau_0$ accounting for delayed heat flux response to temperature gradients [56], and a nonlocal length-scale parameter $\ell_q$ capturing spatial dispersion effects where neighboring regions influence local heat flux.

The generalized form of the GK heat conduction equation is given by [57,58]:

$$\left(1+\tau_0\,\frac{\partial}{\partial t}-\ell_q^2\nabla^2\right)q_i=-K\nabla\theta. \tag{5}$$

This equation captures the temporal delay in heat flux and the spatial nonlocality of thermal interactions, making it particularly effective for modeling heat transfer in nanoscale systems and materials subjected to rapid thermal excitation.

To extend the classical theory of heat conduction in homogeneous isotropic materials, Green and Naghdi [8–10] introduced a set of three thermomechanical formulations, commonly referred to as Type I, Type II, and Type III. The most general of these formulations, Green-Naghdi Type III (GN-III) [9], incorporates both the conventional temperature gradient and an additional thermal displacement gradient, offering a more comprehensive description of heat transport. The constitutive relation for the heat flux vector $q_i$ in the GN-III model is given by [9]:

$$q_i=-\left[K_{ij}\frac{\partial\theta}{\partial x_j}+K_{ij}^*\frac{\partial\psi}{\partial x_j}\right],\ \dot{\psi}=\theta, \tag{6}$$

where $K_{ij}$ and $K_{ij}^*$ are material-dependent conductivity tensors.

Building on this framework, Quintanilla [13,59] introduced a relaxation time parameter $\tau_0$ into the GN-III model to account for delayed thermal responses. This modification leads to an enhanced heat conduction equation that incorporates both spatial and temporal nonlocality [59]:

$$\left(1+\tau_0\,\frac{\partial}{\partial t}\right)q_i=-\left[K_{ij}\frac{\partial\theta}{\partial x_j}+K_{ij}^*\frac{\partial\psi}{\partial x_j}\right]. \tag{7}$$

To further enhance this model by incorporating spatial nonlocality, an essential feature for accurately describing heat conduction in nanoscale systems, the equation can be extended using principles from the GK model. The GK theory introduces a nonlocal length scale parameter $\ell_q$, which accounts for spatial dispersion effects and long-range thermal interactions. By integrating this term into Quintanilla’s formulation, the generalized heat conduction equation becomes [60]:

$$\left(1+\tau_0\,\frac{\partial}{\partial t}-\ell_q^2\nabla^2\right)q_i=-\left[K_{ij}\frac{\partial\theta}{\partial x_j}+K_{ij}^*\frac{\partial\psi}{\partial x_j}\right]. \tag{8}$$

This extended equation combines the temporal relaxation of the GN-III model with the spatial nonlocality of the GK framework, resulting in a powerful and comprehensive description of heat transport. The energy balance equation describes how thermal energy evolves within a deformable medium, accounting for heat conduction and mechanical deformation. It is expressed as [61,62]:

$$\rho C_E\frac{\partial\theta}{\partial t}+T_0\frac{\partial}{\partial t}\left(\beta_{ij}e_{ij}\right)=-q_{i,i}+Q. \tag{9}$$

Fractional derivatives offer a powerful extension of classical differentiation, enabling the modeling of memory effects and anomalous diffusion processes that are prevalent in real-world thermal systems. In 2015, Caputo and Fabrizio [63] introduced a novel fractional derivative characterized by a non-singular exponential kernel, marking a departure from traditional formulations that rely on singular power-law kernels. Their definition aimed to improve the mathematical tractability and physical interpretability of fractional models, particularly in transient heat conduction.

However, in 2016, Atangana and Baleanu [23,24] identified a key limitation in the Caputo-

Fabrizio derivative: It fails to reproduce the original function when the fractional order $\alpha$ approaches zero. To address this issue, they proposed a new formulation based on the Mittag–Leffler function, a generalization of the exponential function that better captures the complex dynamics of fractional systems. The classical Caputo fractional derivative of order $\alpha \in (0,1)$ is defined as [64]:

$$D_C^{\alpha}\mathcal{G}(t)=\frac{1}{\Gamma(1-\alpha)}\int_0^t \frac{1}{(t-u)^{\alpha}}\frac{d\mathcal{G}(u)}{du}du. \tag{10}$$

This definition features a singular kernel at $t=u$, which can pose challenges in numerical implementation and physical interpretation. To overcome this, Caputo and Fabrizio introduced a non-singular exponential kernel, yielding the following formulation [63]:

$$D_{CF}^{\alpha}\mathcal{G}(t)=\frac{1}{1-\alpha}\int_0^t \mathrm{Exp}\left[-\frac{\alpha(t-u)}{(1-\alpha)}\right]\frac{d\mathcal{G}(u)}{du}du,\ \alpha \in (0,1). \tag{11}$$

In contrast, the AB fractional derivative incorporates the Mittag–Leffler function $E_{\alpha}(\cdot)$, which provides a more flexible and accurate representation of memory effects [23,24]:

$$D_{AB}^{\alpha}\mathcal{G}(t)=\frac{1}{1-\alpha}\int_0^t \frac{d\mathcal{G}(u)}{du}E_{\alpha}[-\sigma_{\alpha}(t-u)^{\alpha}]\,du,\ \sigma_{\alpha}=\frac{\alpha}{(1-\alpha)},\alpha \in (0,1). \tag{12}$$

This formulation ensures that the derivative behaves consistently across the full range of $\alpha$, including the limiting case as $\alpha \to 0$, thereby preserving the original function. The Laplace transform of the AB derivative in the Caputo sense is given by [24]:

$$\mathcal{L}[D_{AB}^{\alpha}\mathcal{G}(t)]=\frac{s^{\alpha}\sigma_{\alpha}}{\alpha\sigma_{\alpha}+\alpha s^{\alpha}}. \tag{13}$$

The AB derivative's superiority stems from its non-singular Mittag–Leffler kernel, which models distributed relaxation spectra across multiple timescales, capturing energy barriers at grain boundaries, polymer entanglements, and nanocomposite interfaces. This eliminates the artificial singularities of the Caputo kernel, which unrealistically represent relaxation as localized and instantaneous. For instance, in nanocrystalline metals, the AB kernel accurately describes phonon scattering at grain boundaries with distributed thermal energy storage and release, while Caputo's singularity imposes unrealistic ballistic transport assumptions. Similarly, in fiber-reinforced composites, AB accommodates anisotropic stress relaxation through fiber-matrix debonding and matrix creep, whereas Caputo's singularity induces spurious localized yielding.

Building upon the GK model, researchers have explored fractional extensions to capture nonlocal and memory-dependent thermal behaviors in micro- and nanoscale systems. Early models incorporated the Caputo fractional derivative into the GK framework, introducing temporal nonlocality through fractional-order differentiation.

To enhance physical realism, a novel fractional thermoelastic formulation integrates the AB fractional derivative into the GK model. The AB derivative, with its non-singular Mittag–Leffler kernel, provides superior modeling of memory effects and smooth thermal transitions. This yields the following generalized heat conduction equation [61]:

$$\left(1+\tau_0^{\alpha}\,D_{AB}^{\alpha}-\ell_q^2\nabla^2\right)q_i=-\left(K_{ij}\frac{\partial\theta}{\partial x_j}+K_{ij}^{*}\frac{\partial\psi}{\partial x_j}\right). \tag{14}$$

Combining the energy balance Eq (9) with the fractional nonlocal heat conduction Eq (14) yields a novel MGT-type thermoelastic equation (MGTTE). This model integrates the temporal memory of the AB fractional derivative, the spatial nonlocality of the GK framework, and the thermomechanical coupling of GN-III theory. For isotropic material, the equation is:

$$\begin{gathered}\left(1+\tau_0^\alpha\, D_{AB}^\alpha-\ell_q^2\nabla^2\right)\left[\frac{\partial}{\partial t}\left(\rho C_E\frac{\partial\theta}{\partial t}\right)+T_0\frac{\partial^2}{\partial t^2}\left(\beta_{ij}e_{ij}\right)-\frac{\partial Q}{\partial t}\right]\\ =\frac{\partial}{\partial t}\left(K_{ij}\theta_{,j}\right)_{,i}+\left(K_{ij}^*\theta_{,j}\right)_{,i}.\end{gathered}\tag{15}$$

The final generalized thermoelastic Eq (15) emerges from a systematic fusion of three foundational frameworks. The GK thermoelastic model contributes the spatial nonlocal operator $-\ell^2\nabla^2$, capturing size-dependent thermal dispersion arising from microstructural interactions. The Green–Naghdi Type-III (GN-III) theory provides the dual-conductivity heat flux structure on the right-hand side, combining both instantaneous thermal displacement gradients ($K^*\nabla\theta$) and rate-dependent conduction ($K\,\partial_t\nabla\theta$), enabling the simultaneous modeling of dissipative and undamped thermal waves. Finally, the MGT thermoelastic formulation dictates the left-hand side operator structure, which includes the time derivative of the energy balance equation and ensures finite propagation speed and inherent stability through thermal acceleration terms. By embedding the AB fractional derivative within this hybrid operator, the resulting MGT–GK–GN-III model (Eq (15)) achieves a thermodynamically consistent description that unifies temporal memory, spatial nonlocality, thermal inertia, and dual-mode conduction, offering a comprehensive framework for advanced magneto-thermoelastic analysis.

The formulation markedly improves upon all previous MGT–GK models in three fundamental aspects. First, while classical and integer-order MGT–GK theories successfully remove the paradox of infinite thermal propagation speed and incorporate spatial nonlocality via the $\ell^2\nabla^2$ term, they remain purely local in time and therefore fail to describe memory-dependent hereditary phenomena and anomalous diffusion widely observed in heterogeneous, nanostructured, and polymeric materials. We eliminate this critical limitation by introducing, for the first time, the AB fractional derivative (with non-singular Mittag–Leffler kernel) directly into the MGT–GK heat conduction equation, thereby creating a unified fractional-nonlocal hyperbolic model that simultaneously captures finite wave speed, size-dependent ballistic effects, and long-range temporal memory with tunable fractional order $\alpha\in(0,1)$. Second, the non-singular kernel of the AB operator ensures mathematical and physical consistency across the range of α (including the limiting cases $\alpha\to 0$ and $\alpha\to 1$), avoids the singularities inherent in Caputo-based formulations, and yields significantly smoother and more realistic field distributions than any prior integer-order or singular-kernel MGT–GK approach. Third, the model is consistently generalized to transversely isotropic magneto-thermoelasticity in hollow annular cylinders, a geometrically relevant and technologically important configuration that has never before been analyzed within the MGT–GK framework. These combined extensions provide a substantially more general, stable, and predictive theoretical tool for complex modern materials under extreme transient conditions than any published MGT–GK model.

## 3. Electromagnetic and Maxwell's equations

The electromagnetic response of the conducting, slowly moving, deformable transversely isotropic medium subjected to a uniform initial magnetic field $\vec{H}_0$ is governed by Maxwell's equations in the quasi-static approximation together with the generalized Ohm's law. Assuming negligible free charge density ($\rho_{\mathrm{e}} = 0$) and neglecting the displacement current (valid for the low-to-moderate frequencies typical of thermoelastic waves), Maxwell's equations simplify to the following form commonly employed in magneto-thermoelasticity [36,37]:

$$\begin{gathered} \vec{J} = \nabla \times \vec{h} + \frac{\partial \vec{D}}{\partial t},\ \nabla \times \vec{E} = -\mu_0 \frac{\partial \vec{B}}{\partial t}, \vec{B} = \mu_0 \vec{H},\ \vec{D} = \varepsilon_0 \vec{E}, \\ \vec{H} = \vec{H}_0 + \vec{h},\ \ \nabla \cdot \vec{h} = 0,\ \ \nabla \cdot \vec{D} = 0. \end{gathered} \tag{16}$$

The electromagnetic stress within the medium is quantified using the Maxwell stress tensor $\tau_{ij}$, which captures the mechanical influence of the magnetic field [64]:

$$\tau_{ij} = \mu_0 \left[ H_i h_j + H_j h_i - H_k h_k \delta_{ij} \right]. \tag{17}$$

This tensor contributes to the total stress state and magnetoelastic coupling, particularly in materials under strong magnetic fields. When the influence of the temperature gradient on the current density $\vec{J}$ is neglected, the generalized Ohm's law for a deformable continuum can be expressed as [65]:

$$\vec{J} = \sigma_0 \left[ \vec{E} + \frac{\partial \vec{u}}{\partial t} \times \vec{B} \right]. \tag{18}$$

This formulation incorporates the electromotive force from medium motion in magnetic fields, the magnetoelastic effect. Electrical conductivity $\sigma_0$ governs current conduction in materials. While metals like copper and silver have high conductivity, perfect conductivity ($\sigma_0 \to \infty$) remains theoretical. All real materials have finite resistance, including superconductors under specific conditions. Perfect conductivity simplifies models when resistance is negligible, but realistic simulations must consider finite, material-dependent $\sigma_0$ values that affect current distribution, Joule heating, and electromagnetic propagation.

The applied uniform magnetic field $\vec{H}_0$ generates Lorentz body forces that oppose radial expansion, thereby reducing displacement and stress amplitudes while inducing eddy currents that contribute additional Joule heating.

## 4. Formulation of the problem

We consider an infinitely long, hollow, elastic cylinder composed of a transversely isotropic material with finite electrical conductivity. The geometry is described using cylindrical polar coordinates $(r, \Theta, z)$, where the $z$-axis coincides with the cylinder's axis of symmetry. The cylinder has inner and outer radii denoted by $a$ and $b$, respectively, with subscripts 1 and 2 referring to the inner and outer surfaces (see Figure 1).

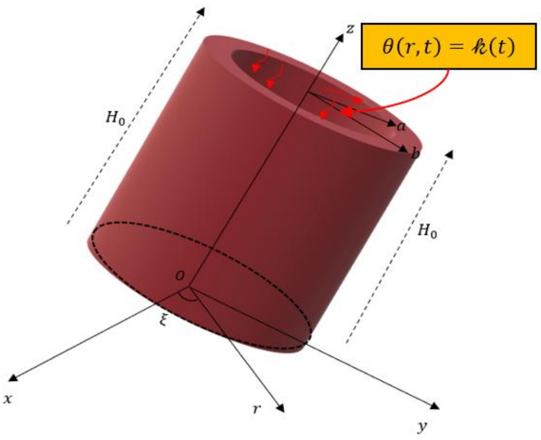

**Figure 1.** Illustrative diagram depicting the thermoelastic response of a hollow cylinder.

The inner surface $(r = a)$ is assumed to be traction-free and subjected to a time-dependent thermal environment, while the outer surface $(r = b)$ is thermally insulated and mechanically unloaded. Due to the axial symmetry and infinite extent of the cylinder, all field variables depend solely on the radial coordinate $r$ and time $t$. Consequently, the displacement vector takes the simplified form:

$$\vec{u} = (u_r, u_\Theta, u_z) = (u(r,t), 0, 0). \tag{19}$$

For axisymmetric problems, the stress–strain–temperature relations are given by:

$$\begin{aligned} \sigma_{rr} &= c_{11}\varepsilon_{rr} + c_{12}\varepsilon_{\xi\xi} + c_{13}\varepsilon_{zz} - \beta_{rr}\theta, \\ \sigma_{\xi\xi} &= c_{12}\varepsilon_{rr} + c_{11}\varepsilon_{\xi\xi} + c_{13}\varepsilon_{zz} - \beta_{\Theta\Theta}\theta, \\ \sigma_{zz} &= c_{13}\varepsilon_{rr} + c_{13}\varepsilon_{\xi\xi} + c_{33}\varepsilon_{zz} - \beta_{zz}\theta, \\ \sigma_{rz} &= 2c_{44}\varepsilon_{rz}. \end{aligned} \tag{20}$$

These relations can be reduced to those of an isotropic thermoelastic material by setting: $c_{11} = c_{22} = \lambda + 2\mu,\ c_{12} = c_{13} = \lambda,\ c_{44} = \mu,\ \beta_{11} = \beta_{22} = \beta_{33}$.

The strain–displacement relations for axisymmetric deformations reduce to:

$$\varepsilon_{rr} = \frac{\partial u_r}{\partial r}\ , e_{\Theta\Theta} = \frac{u_r}{r},\ e_{rz} = 0,\ e_{zz} = 0, e_{r\Theta} = 0, e_{z\Theta} = 0. \tag{21}$$

In the presence of body forces, the equation of motion in cylindrical coordinates takes the form:

$$\frac{\partial \sigma_{rr}}{\partial r} + \frac{1}{r}(\sigma_{rr} - \sigma_{\Theta\Theta}) + F_r = \rho\frac{\partial^2 u_r}{\partial t^2}. \tag{22}$$

Substituting Eqs (20) and (21) into (22) gives the displacement-based motion equation for axisymmetric configurations:

$$c_{11}\left(\frac{\partial^2 u_r}{\partial r^2} + \frac{1}{r}\frac{\partial u_r}{\partial r} - \frac{u_r}{r^2}\right) + F_r = \beta_{rr}\frac{\partial \theta}{\partial r} + \frac{(\beta_{rr} - \beta_{\Theta\Theta})}{r}\theta + \rho\frac{\partial^2 u}{\partial t^2}. \tag{23}$$

For transversely isotropic materials, it holds that $\beta_{rr} = \beta_{\Theta\Theta}$, which simplifies the thermal coupling term. Thus, the equation of motion becomes:

$$c_{11}\left(\frac{\partial^2 u_r}{\partial r^2}+\frac{1}{r}\frac{\partial u_r}{\partial r}-\frac{u_r}{r^2}\right)+F_r=\beta_{rr}\frac{\partial\theta}{\partial r}+\rho\frac{\partial^2 u}{\partial t^2}. \tag{24}$$

A static magnetic field $\vec{H}_0=(0,0,H_0)$ is applied axially. The conducting medium's motion induces secondary electromagnetic fields: A small magnetic field $\vec{h}=(0,0,h)$ and electric field $\vec{E}=(0,E,0)$, with current density $\vec{J}=(0,J,0)$. From linearized Ohm's law:

$$J=\sigma_0\left(-\mu_0 H_0\frac{\partial u}{\partial t}+E\right). \tag{25}$$

Maxwell's equations (neglecting displacement current in the conductor) yield:

$$-\mu_0\frac{\partial h}{\partial t}=\frac{1}{r}\frac{\partial}{\partial r}(rE),\quad \frac{\partial h}{\partial r}=-\varepsilon_0\frac{\partial E}{\partial t}-J. \tag{26}$$

In the vacuum surrounding the cylinder, the magnetic field induces electric and magnetic fields ($h^0$ and $E^0$) satisfying:

$$\frac{1}{r}\frac{\partial}{\partial r}(rE^0)=-\mu_0\frac{\partial h^0}{\partial t},\ \frac{\partial h^0}{\partial r}=-\varepsilon_0\frac{\partial E^0}{\partial t}. \tag{27}$$

Here, $E^0$ and $h^0$ denote the Θ-components of the electric field intensity and induced magnetic field in the external vacuum. Eliminating $J$ from Eqs (25) and (26) leads to:

$$\frac{\partial h}{\partial r}=\sigma_0\mu_0 H_0\frac{\partial u}{\partial t}-\left(\sigma_0 E+\varepsilon_0\frac{\partial E}{\partial t}\right). \tag{28}$$

Further eliminating $E$ from Eqs (26) and (28) results in:

$$\left(\nabla^2-\mu_0\varepsilon_0\frac{\partial^2}{\partial t^2}-\mu_0\sigma_0\frac{\partial}{\partial t}\right)h=\mu_0\sigma_0 H_0\frac{\partial e}{\partial t}, \tag{29}$$

where $\nabla^2=\frac{\partial^2}{\partial r^2}+\frac{1}{r}\frac{\partial}{\partial r}$ is the axisymmetric Laplacian, and by $e=e_{rr}+e_{\Theta\Theta}+e_{zz}=\frac{1}{r}\frac{\partial}{\partial r}(ru)$ is the cubical dilatation.

Applying Eq (17), the radial Maxwell stress tensor component is:

$$\tau_{rr}=-H_0\mu_0 h. \tag{30}$$

From Eq (23), the Lorentz force exhibits a single $r$-component:

$$F_r=\left(\vec{J}\times\vec{B}\right)_r=-H_0\mu_0\frac{\partial h}{\partial r}. \tag{31}$$

Incorporating Eqs (31) and (24), the motion equation becomes:

$$c_{11}\left(\left(\frac{\partial}{\partial r}+\frac{1}{r}\right)\left(\frac{\partial}{\partial r}\right)-\rho\frac{\partial^2}{\partial t^2}\right)u=\beta_{rr}\frac{\partial\theta}{\partial r}+\mu_0 H_0\frac{\partial h}{\partial r}. \tag{32}$$

Applying the divergence operator and using $\mathrm{e}=\frac{1}{r}\frac{\partial}{\partial r}(ru)$, we obtain:

$$\left(c_{11}\nabla^2 - \rho\frac{\partial^2}{\partial t^2}\right)e = \beta_{rr}\nabla^2\theta + H_0\mu_0\nabla^2 h. \tag{33}$$

The thermal behavior is governed by a generalized nonlocal heat conduction model based on the MGT heat equation, enhanced with the AB fractional derivative of order $\alpha \in (0,1]$. The resulting energy equation reads:

$$\left(1 + \tau_0^{\alpha}\, D_{AB}^{\alpha} - \ell_q^2\nabla^2\right)\left(\rho C_E\frac{\partial^2\theta}{\partial t^2} + T_0\beta_{rr}\frac{\partial^2 e}{\partial t^2}\right) = \left(K\frac{\partial}{\partial t} + K^*\right)\nabla^2\theta. \tag{34}$$

## 5. Dimensionless formulation of governing equations

To enable analytical tractability and highlight dominant magneto-thermoelastic coupling mechanisms, the governing equations are recast in dimensionless form using these variables:

$$\begin{gathered}\{u', r', a', b'\} = v_0\eta_0\{u, r, a, b\},\ \{t', \tau_0'\} = v_0^2\eta_0\{t, \tau_0\},\ \theta' = \frac{\theta}{T_0}, \sigma_{ij}' = \frac{\sigma_{ij}}{c_{11}},\\ \ell_q' = v_0\eta_0\ell_q, \tau_{ij}' = \frac{\tau_{ij}}{c_{11}},\ h' = \frac{\omega\varphi}{\sigma_0\mu_0 H_0}h,\ E' = \frac{\omega}{\vartheta\sigma_0\mu_0^2 H_0}E,\ v_0^2 = \frac{c_{11}}{\rho}, \eta_0 = \frac{\rho C_E}{K}.\end{gathered} \tag{35}$$

For convenience, we drop prime notation from dimensionless variables. Substituting these transformations, the governing Eqs (27)–(30) and (34) become the following unit-free dimensionless forms:

$$\frac{\partial u}{\partial t} = \left(\mathscr{v}^2\frac{\partial}{\partial t} + \mathcal{P}_0\right)E + \frac{\partial h}{\partial r}, \tag{36}$$

$$\left(\nabla^2 - \mathscr{v}^2\frac{\partial^2}{\partial t^2} - \mathcal{P}_0\frac{\partial}{\partial t}\right)h = \frac{\partial e}{\partial t}, \tag{37}$$

$$\begin{gathered}-\frac{\partial h^0}{\partial r} = \mathscr{v}^2\frac{\partial E^0}{\partial t},\\ -\frac{\partial h^0}{\partial t} = \frac{1}{r}\frac{\partial}{\partial r}(rE^0),\end{gathered} \tag{38}$$

$$\left(\nabla^2 - \frac{\partial^2}{\partial t^2}\right)e = \mathcal{Q}_1\nabla^2\theta + m_0\mathcal{Q}_2\nabla^2 h, \tag{39}$$

$$\left(1 + \tau_0^{\alpha}\, D_{AB}^{\alpha} - \ell_q^2\nabla^2\right)\left(\frac{\partial^2\theta}{\partial t^2} + \mathcal{Q}_1\frac{\partial^2 e}{\partial t^2}\right) = \frac{\partial}{\partial t}\nabla^2\theta + \mathcal{Q}_3\nabla^2\theta, \tag{40}$$

where

$$\mathcal{P}_0 = \frac{\sigma_0\mu_0}{\omega}, \mathscr{v} = \frac{v_0}{c_L}, c_L = \sqrt{\frac{1}{\mu_0\varepsilon_0}}, \mathcal{Q}_1 = \frac{T_0\beta_{rr}}{c_{11}}, \mathcal{Q}_2 = \frac{H_0\mu_0}{\rho\, v_0^2}, \mathcal{Q}_3 = \frac{K^*}{v_0^2 K}. \tag{41}$$

Parameter $\mathcal{P}_0$ quantifies magnetic damping from eddy currents induced by motion in the magnetic field, while $\mathscr{v}$ reflects relative mechanical-electromagnetic propagation speeds. The speed of light $c_L$ emerges from Maxwell's equations in free space. Setting $\mathcal{P}_0 = 0$, $\mathscr{v}^2 = 0$, and $\delta_2 = 0$ (eliminating electromagnetic effects via $\sigma_0 \to 0$ or $H_0 \to 0$) reduces the system to classical generalized thermoelasticity without magneto-electric coupling, confirming this framework properly extends existing theories.

The dimensionless stress–strain–temperature constitutive laws yield mechanical stress components and Maxwell stress as:

$$\begin{aligned} \sigma_{rr} &= \frac{\partial u}{\partial r} + c_1 \frac{u}{r} - Q_1 \theta, \\ \sigma_{\xi\xi} &= c_1 \frac{\partial u}{\partial r} + \frac{u}{r} - Q_1 \theta, \\ \sigma_{zz} &= c_2 \frac{\partial u}{\partial r} + c_2 \frac{u}{r} - Q_4 \theta, \end{aligned} \tag{42}$$

$$\tau_{rr} = -Q_2 \mathcal{P}_0 h, \tag{43}$$

where

$$c_1 = \frac{c_{12}}{c_{11}},\ c_2 = \frac{c_{13}}{c_{11}},\ Q_3 = \frac{T_0 \beta_{rr}}{c_{11}},\ Q_4 = \frac{T_0 \beta_{zz}}{c_{11}}. \tag{44}$$

## 6. Conditions boundary and initial conditions

The physical scenario under investigation assumes that the hollow cylindrical medium is initially undisturbed, i.e., at rest and in thermal equilibrium with its surroundings. Consequently, all field variables vanish at the initial instant $t = 0$. This leads to the following initial conditions:

$$u(r,0) = 0 = \dot{u}(r,0),\quad \theta(r,0) = 0 = \dot{\theta}(r,0), \sigma_{ii}(r,0) = 0. \tag{45}$$

The hollow cylinder experiences time-varying thermal loading on its traction-free inner surface $(r = a)$ through a bi-exponential thermal pulse [66]:

$$\theta(r,t) = \mathcal{k}(t) = \theta_0 \left(\beta \mathrm{e}^{-\gamma_1 t} + (1-\beta)\mathrm{e}^{-\gamma_2 t}\right) H(t) \quad \text{at} \quad r = a, \tag{46}$$

where $\theta_0$ is the peak thermal amplitude, $\gamma_1$ and $\gamma_2$ $(\geq 0)$ are decay rates for two thermal relaxation mechanisms, $\beta$ $(0 \leq \beta \leq 1)$ weights the first decay mode, and $H(t)$ is the Heaviside function.

This condition generalizes transient thermal excitation. When $\beta = 1$ and $\gamma_1 = \gamma_2 = 0$, it reduces to $\theta(R_1, t) = \theta_0\, H(t)$, the classical thermal shock condition. The bi-exponential formulation thus encompasses multi-timescale thermal loading and idealized thermal shock, providing flexibility for pulsed heating, laser irradiation, or rapid thermal cycling applications.

The mechanically traction-free inner surface requires:

$$\sigma_{rr}(r,t) = 0 \qquad \text{at} \qquad r = a. \tag{47}$$

The outer surface $(r = b)$ is thermally insulated and mechanically unloaded, giving:

$$\frac{\partial \theta(r,t)}{\partial r} = 0 \quad \text{at} \quad r = b, \tag{48}$$

$$\sigma_{rr}(r,t) = 0 \quad \text{at} \quad r = b. \tag{49}$$

Electromagnetic field continuity at the material-vacuum interfaces requires:

$$E(r,t) = E^0(r,t) \quad \text{at} \quad r = a, b, \tag{50}$$

$$h(r,t) = h^0(r,t) \quad \text{at} \quad r = a, b. \tag{51}$$

These conditions satisfy Maxwell's equations globally and prevent spurious surface currents or discontinuities.

## 7. Analytical solution techniques

Applying the Laplace transform (denoted by overbar, e.g., $\bar{\mathcal{F}}(r,s)=\mathcal{L}\{\mathcal{F}(r,t)\}$) to the dimensionless governing equations yields:

$$\begin{gathered}(\nabla^2-s^2)\bar{e}=\mathcal{Q}_1\nabla^2\bar{\theta}+\mathcal{Q}_2\nabla^2\bar{h},\\ \mathcal{Q}_1(\mathcal{Q}_5-\mathcal{Q}_6\nabla^2)\bar{e}=\big((1+\mathcal{Q}_6)\nabla^2-\mathcal{Q}_5\big)\bar{\theta},\\ (\nabla^2-\varphi_2)\bar{h}=s\bar{e},\end{gathered} \tag{52}$$

$$\begin{gathered}\frac{d\bar{h}}{dr}=s\bar{u}-\varphi_1\bar{E},\\ \frac{dh^0}{dr}=-s\upsilon^2\bar{E}^0,\\ \frac{1}{r}\frac{d}{dr}(r\bar{E}^0)=-s\bar{h}^0,\end{gathered} \tag{53}$$

$$\begin{gathered}\sigma_{rr}=\frac{d\bar{u}}{dr}+c_1\frac{\bar{u}}{r}-\mathcal{Q}_1\bar{\theta},\\ \sigma_{\xi\xi}=c_1\frac{d\bar{u}}{dr}+\frac{\bar{u}}{r}-\mathcal{Q}_1\bar{\theta},\\ \sigma_{zz}=c_2\frac{d\bar{u}}{dr}+c_2\frac{\bar{u}}{r}-\mathcal{Q}_4\bar{\theta},\end{gathered} \tag{54}$$

$$\bar{\tau}_{rr}=-\mathcal{Q}_2\mathcal{P}_0\bar{h}, \tag{55}$$

where

$$\varphi_1=\mathcal{P}_0+s\upsilon^2,\ \ \varphi_2=s\varphi_1,\mathcal{Q}_5=\frac{s^2}{s+\mathcal{Q}_3}\left(1+\frac{\mu_\alpha s^\alpha}{\alpha\mu_\alpha+\alpha s^\alpha}\right),\mathcal{Q}_6=\frac{s^2\ell_q^2}{s+\mathcal{Q}_3}. \tag{56}$$

Eliminating $\bar{\theta}$ and $\bar{h}$ from Eq (52) yields:

$$(\nabla^6-A\nabla^4+B\nabla^2-C)\bar{e}(r,s)\ =0, \tag{57}$$

where

$$\begin{gathered}A=\frac{\mathcal{Q}_5+\mathcal{Q}_8\mathcal{Q}_7+\mathcal{Q}_1^2\mathcal{Q}_5}{\mathcal{Q}_7+\mathcal{Q}_1^2\mathcal{Q}_6},\quad B=\frac{\mathcal{Q}_5\mathcal{Q}_8+s^2\varphi_2\mathcal{Q}_7-\varphi_2\mathcal{Q}_6\mathcal{Q}_1^2}{\mathcal{Q}_7+\mathcal{Q}_1^2\mathcal{Q}_6}\ ,\quad C=\frac{\mathcal{Q}_5\varphi_2s^2}{\mathcal{Q}_7+\mathcal{Q}_1^2\mathcal{Q}_6},\\ \delta_7=1+\mathcal{Q}_6,\mathcal{Q}_8=s^2+\varphi_2+s\mathcal{Q}_2.\end{gathered} \tag{58}$$

This sixth-order operator can be factorized into a product of three second-order Helmholtz-type operators:

$$(\nabla^2-m_1^2)(\nabla^2-m_2^2)(\nabla^2-m_3^2)\bar{e}(r,s)\ =0, \tag{59}$$

where $m_1^2$, $m_2^2$, and $m_3^2$ are roots of the characteristic polynomial:

$$m^6-Am^4+Bm^2-C\ =0. \tag{60}$$

For axisymmetric cylindrical geometry, the general solution uses modified Bessel functions:

$$\bar{e}(r,s) = \sum_{i=1}^{3}\big(A_i I_0(m_i r) + B_i K_0(m_i r)\big). \tag{61}$$

The six coefficients $A_i$ and $B_i$ $(i = 1, 2, 3)$ are $s$-dependent and determined from boundary conditions. Using constitutive and kinematic relations in the Laplace domain, $\bar{\theta}(r,s)$ and $\bar{h}(r,s)$ are expressed with the same Bessel basis:

$$\begin{aligned}\bar{\theta}(r,s) &= \sum_{i=1}^{3}\big(A_i' I_0(m_i r) + B_i' K_0(m_i r)\big),\\ \bar{h}(r,s) &= \sum_{i=1}^{3}\big(A_i'' I_0(m_i r) + B_i'' K_0(m_i r)\big).\end{aligned} \tag{62}$$

Algebraic relations (52) impose proportionality constraints between field coefficients:

$$\{A_i', B_i'\} = \left(\frac{\mathcal{Q}_1(\mathcal{Q}_5 - \mathcal{Q}_6 m_i^2)}{(1+\mathcal{Q}_6)m_i^2 - \mathcal{Q}_5}\right)\{A_i, B_i\},\ \{A_i'', B_i''\} = \left(\frac{s}{m_i^2 - \varphi_2}\right)\{A_i, B_i\}, i = 1,2,3. \tag{63}$$

The radial displacement $\bar{u}$ is obtained by solving the first-order ODE derived from the dilatation definition $\bar{e} = \frac{1}{r}\left(\frac{d}{dr}r\bar{u}\right)$, yielding:

$$\bar{u} = \sum_{i=1}^{3}\frac{1}{m_i}\big(A_i I_1(m_i r) - B_i K_1(m_i r)\big), \tag{64}$$

where $I_1(m_i r)$ and $K_1(m_i r)$ are modified Bessel functions of the first and second kinds, respectively, with order one. Substituting $\bar{u}$ and $\bar{h}$ into the transformed electromagnetic relation (53) provides the induced electric field $\bar{E}$ within the solid:

$$\bar{E} = -s^2\sum_{i=1}^{3}\frac{1}{m_i(m_i^2 - s\varphi_2)}(A_i I_1(m_i r) - B_i K_1(m_i r)). \tag{65}$$

For the surrounding vacuum, the electromagnetic fields $\bar{E}^0$ and $\bar{h}^0$ satisfy the decoupled system (53). Eliminating $\bar{E}^0$ leads to a modified Helmholtz equation for $\bar{h}^0$:

$$(\nabla^2 - s^2 v^2)\bar{h}^0 = 0. \tag{66}$$

To ensure a physically meaningful solution, bounded at $r \to 0$ and $r \to \infty$, the domain is split into two regions. In the interior ($r < R_2$), the solution must be finite at the cylinder's center, using only the modified Bessel function $I_0$. In the exterior ($r > R_1$), the field must vanish as $r \to \infty$, using only the modified Bessel function $K_0$. The vacuum field solutions are expressed accordingly:

$$\begin{aligned}\bar{h}^{01} &= A_4 I_0(svr),\\ \bar{h}^{02} &= A_5 K_0(svr),\\ \bar{E}^{01} &= -\frac{1}{v}A_4 I_1(svr),\\ \bar{E}^{02} &= \frac{1}{v}A_4 K_1(svr),\end{aligned} \tag{67}$$

where $A_4$ and $A_5$ are integration constants determined by continuity conditions (50) and (51). Substituting $\bar{\theta}(r,s)$ and $\bar{u}(r,s)$ into dimensionless constitutive relations (54) gives closed-form expressions for the transformed stress components. The radial component of the Maxwell stress tensor can be derived as:

$$\bar{\tau}_{rr} = -Q_2 m_0 \sum_{i=1}^{3}\left(\frac{s}{m_i^2-\varphi_2}\right)(A_i I_0(m_i r) + B_i K_0(m_i r). \tag{68}$$

To find the twelve unknown coefficients $A_i$ and $B_i$ $(i = 1, 2, 3)$, the boundary conditions (46)–(51) are transformed into the Laplace domain as:

$$\begin{gathered}\bar{\theta}(a,s) = \theta_0\left(\frac{\beta}{\gamma_1+s}+\frac{1-\beta}{\gamma_2+s}\right),\\ \left.\frac{d\bar{\theta}(r,s)}{dr}\right|_{r=b},\\ \bar{\sigma}_{rr}(a,s) = 0,\ \ \bar{\sigma}_{rr}(b,s) = 0,\end{gathered} \tag{69}$$

$$\begin{gathered}\bar{E}(a,s) = \bar{E}^{01}(a,s),\ \ \bar{h}(a,s) = \bar{h}^{01}(a,s),\\ \bar{E}(b,s) = \bar{E}^{02}(b,s), \bar{h}(b,s) = \bar{h}^{02}(b,s).\end{gathered} \tag{70}$$

Applying the defined boundary conditions yields two systems of linear equations for the undetermined constants $A_i$, and $B_i$ $(i = 1, 2, 3)$, solved using continuity and compatibility conditions at the interfaces. This provides a unified solution in the Laplace transform domain. To obtain the physical behavior, inverse Laplace transforms are applied to express fields in the space-time domain. Analytical inversion is often infeasible for complex systems with coupled PDEs, fractional derivatives, and nonlocal effects, making numerical inversion techniques essential for recovering time-domain solutions.

## 8. Limiting cases and physical consistency of the model

To confirm the correctness and generality of the proposed fractional-nonlocal MGT–GK model, the following physically meaningful limiting cases are examined:

### *8.1. Fractional order* $\alpha \to 1$

When $\alpha = 1$, the Atangana–Baleanu fractional derivative reduces exactly to the ordinary first-order time derivative (see Eq (12) and the Laplace transform property in Eq (13)). Consequently, the final heat conduction Eq (15) and the entire system revert to the integer-order nonlocal MGT–GK model with spatial nonlocality $\ell_q \neq 0$, which has been validated in numerous studies for nanoscale heat transport.

### *8.2. Nonlocal length scale* $\ell_q \to 0$

Setting $\ell_q = 0$ eliminates the $\ell_q^2\nabla^2 q$ term, thereby recovering the purely temporal (local in space) fractional MGT model without size-dependent effects. This limit correctly describes heat conduction in bulk materials where characteristic lengths are much larger than phonon mean free paths, and the results coincide with recent fractional MGT formulations for isotropic and anisotropic solids.

### *8.3. Applied magnetic field* $H_0 \to 0$

When the uniform magnetic field vanishes ($H_0 = 0$), the Lorentz force terms disappear, the induced electric and magnetic fields ($E$ and $h$) become zero, and Maxwell's equations decouple from the thermoelastic system. The governing equations then reduce to the purely fractional-nonlocal thermoelastic problem without electromagnetic interaction, consistent with earlier non-magnetic fractional GK and MGT studies.

### 8.4. Combined limit $\alpha \to 1$ and $\ell_q \to 0$

This simultaneous limit recovers the classical integer-order, local (Fourier-based) Lord–Shulman or GN-III magneto-thermoelastic models (depending on the retained relaxation parameters), thereby confirming compatibility with the most widely accepted generalized theories.

### 8.5. Combined limit $\alpha \to 1$, $\ell_q \to 0$, and $H_0 \to 0$

Simultaneously taking $\alpha \to 1$, $\ell_q \to 0$, and $H_0 \to 0$ collapses the model to classical coupled thermoelasticity (Biot's theory); retaining $\tau_0 \neq 0$ gives the Lord–Shulman model, while keeping $K^* \neq 0$ recovers GN-III. These hierarchical reductions confirm that the present formulation is thermodynamically consistent and mathematically coherent, embedding established theories as exact sub-cases while extending them to capture memory, nonlocality, and electromagnetic coupling in advanced materials.

## 9. Numerical inversion of Laplace transforms

Various numerical methods, such as the Euler method, Talbot algorithm, Stehfest approach, and Fourier series-based techniques [67–69], approximate the inverse Laplace transform with differing accuracy, stability, and computational costs. In this section, we present a Fourier series-based numerical method to compute the inverse Laplace transform for physical fields, featuring simple, repetitive operations ideal for digital implementation. The Fast Fourier Transform (FFT) is used to enhance efficiency [70]. For a given time $t$ and positive parameter $\xi$, the approximate function $\mathcal{F}(r,t)$ is [70]:

$$\mathcal{F}(r,t)=\frac{e^{\xi t}}{t_1}\left(\frac{1}{2}\bar{\mathcal{F}}(r,\xi)+\mathcal{R}\left[\sum_{n=1}^{m} \mathrm{e}^{\frac{int\pi}{t_1}}\bar{\mathcal{F}}\left(r,\xi+\frac{in\pi}{t_1}\right)\right]\right), \tag{71}$$

where $t_1$ sets the Fourier expansion period ($t \leq 2t_1$), $\xi > 0$ shifts the Bromwich contour right of all singularities of $\bar{\mathcal{F}}(r,s)$, $m$ is the number of terms in the truncated series (affecting accuracy), and $\mathcal{R}[\cdot]$ denotes the real part. Accuracy depends on the convergence region, numerical method, and function complexity. Sensitivity analyses and error assessments are crucial for reliable results, particularly in selecting $\xi$ to control the error term $\mathrm{e}^{-2\xi t_1}\bar{f}(r,t+2nt_1)$ in Eq (75) [70].

In this study, the Dubner–Abate parameters are carefully calibrated through a convergence analysis. The Bromwich shift parameter is set to $\xi = 5.0$, based on spectral analysis of the transformed system, ensuring the integration contour lies to the right of all poles (which are concentrated near $\mathcal{R}(\mathrm{s}) \approx 1.2$). The half-period $t_1$ is chosen equal to the observation time ($t_1 = t = 0.25$), satisfying the stability condition $t \leq 2t_1$. The number of Fourier terms $m = 40$ is selected after testing values from 30 to 50: Beyond $m = 40$, the relative change in all field variables is less than 0.8%, confirming numerical convergence. This parameter set ensured high accuracy while avoiding Gibbs-type oscillations and exponential error amplification, which is consistent with established practices in generalized thermoelasticity.

## 10. Numerical results and analysis

In this section, we evaluate the performance, physical consistency, and predictive capability of the fractional nonlocal MGT thermoelastic model (FN-MGT) through comprehensive numerical simulations. The results are compared across fractional operators and classical limits to highlight the effects of memory, nonlocality, and electromagnetic coupling on the thermoelastic response of advanced materials.

Cobalt (Co) is chosen as the reference material due to its high-temperature stability, mechanical strength, and magnetic responsiveness, making it ideal for applications in aerospace, nuclear reactors, turbines, and electromagnetic shielding. Its ability to withstand severe thermal gradients supports reliable analysis of coupled thermal–mechanical–magnetic interactions. Numerical simulations of the physical properties of cobalt are listed in SI units in Table 1.

**Table 1.** Thermal–mechanical–magnetic physical properties of cobalt [71,72].

| Property | Symbol | Value | Units |
|---|---|---|---|
| Elastic constants | $c_{11}$ | $2.49 \times 10^{11}$ | N/m² |
| | $c_{12}$ | $1.41 \times 10^{11}$ | N/m² |
| | $c_{13}$ | $1.03 \times 10^{11}$ | N/m² |
| | $c_{33}$ | $2.81 \times 10^{11}$ | N/m² |
| Density | $\rho$ | $8900$ | kg/m³ |
| Thermoelastic coupling coefficients | $\beta_{rr}$ | $3.58 \times 10^{6}\}$ | N/(K·m²) |
| | $\beta_{zz}$ | $4 \times 10^{6}$ | N/(K·m²) |
| Specific heat at constant strain | $C_E$ | $420$ | J/(kg·K) |
| Reference temperature | $T_0$ | $293$ | K |
| Electric permittivity (vacuum) | $\varepsilon_0$ | $8.854 \times 10^{-12}$ | F/m |
| Magnetic permeability (vacuum) | $\mu_0$ | $1.2571 \times 10^{-6}$ | H/m |
| Applied magnetic field intensity | $H_0$ | $0.795 \times 10^{6}$ | A/m |
| Dimensionless temperature amplitude | $\theta_0 = 1$ | 1 | — |
| Dimensionless thermal relaxation time | $\tau_0$ | $0.02$ | — |
| Electrical conductivity | $\sigma_0$ | $1.6 \times 10^{7}$ | Ω⁻¹·m⁻¹ |
| Thermal conductivity | $K$ | $69$ | W/(m·K) |
| Nonlocal thermal conductivity rate | $K^{*}$ | 2 | W/(s·m·K) |
| Dimensionless inner radius | $a$ | 1 | — |
| Dimensionless outer radius | $b$ | 2 | — |

Table 2 summarizes the simulation parameters and their respective ranges used in the parametric studies illustrated in Figures 2–15. A parametric analysis evaluates the system's response to variations in the internal length-scale parameter ($\ell_q$) within the GK framework. The analysis compares two fractional operators: the AB fractional derivative, using a non-singular, non-local Mittag–Leffler kernel, and the classical Caputo (C) derivative, with a singular power-law kernel. Additionally, the limiting case of fractional order $\alpha = 1$, corresponding to standard integer-order derivatives, is considered.

**Table 2.** Summary of simulation parameters and ranges used in Figures 2–15.

| Figure Set | Studied Parameter | Values / Operators Tested | Fixed Parameters |
|---|---|---|---|
| Figs. 2–8 | Nonlocal length scale $\ell_q$ | 0, 0.01, 0.03, 0.05, 0.07, 0.09 | $\alpha = 0.75$, AB operator, $\tau_0 = 0.05$ |
| Figs. 9–15 | Fractional order $\alpha$ and operator type | $\alpha = 80, 0.85, 0.90$ (AB and Caputo); $\alpha =$ 1(integer-order) | $\ell_q = 0.05,\ \tau_0 = 0.02$ |
| All figures | Geometry & time | $R_1 = 1,\ R_2 = 2,\ t = 0.25$ | — |
| All figures | Material | Cobalt (properties in Table 1) | — |

### 10.1. *Influence of nonlocal thermal length-scale parameter ($\ell_q$)*

The nonlocal thermal length-scale parameter $\ell_q$, embedded in the fractional nonlocal MGT heat conduction model (FN-MGT), serves as a critical measure of the spatial range over which thermal interactions occur. Physically, $\ell_q$ accounts for microstructural features, such as grain boundaries, defects, or phonon mean free paths, that become significant in micro- and nanoscale systems, where classical Fourier-based theories fail to capture size-dependent thermal behavior. By introducing spatial nonlocality, this parameter effectively models the influence of neighboring regions on local heat flux, thereby generalizing the heat conduction law beyond the assumption of purely local and instantaneous thermal response.

In this subsection, we investigate the impact of varying $\ell_q$ on the thermoelastic field variables within a transversely isotropic hollow cylinder. We consider six values of the nonlocal parameter $\ell_q \in \{0, 0.01, 0.03, 0.05, 0.07, 0.09\}$, while fixing the fractional order at $\alpha = 0.75$ and the thermal relaxation time at $\tau_0 = 0.05$. The selected range spans from the classical local limit ($\ell_q = 0$) to progressively stronger nonlocal effects. The computed responses, namely, the temperature distribution $\theta$, radial displacement $u$, and thermal stress components $\sigma_{rr}$ and $\sigma_{\Theta\Theta}$, are evaluated over the radial domain $1 \le r \le 2$ and presented in Figures 2–6. The results confirm that $\ell_q$ acts as a regularization parameter that captures the intrinsic microstructural resistance to abrupt thermal and mechanical changes.

Numerical results show that the nonlocal thermal length-scale parameter ($\ell_q$) significantly alters the thermoelastic response of transversely isotropic hollow cylinders by introducing spatial nonlocality in heat transfer dynamics. As $\ell_q$ increases from 0 (classical local limit) to 0.09, microstructural resistance to thermal and mechanical perturbations grows, markedly affecting field distributions. This discussion integrates these findings, highlighting their mechanistic origins and engineering implications.

Figure 2 shows that increasing the nonlocal thermal length-scale parameter ($\ell_q$) enhances spatial smoothing and reduces peak temperature ($\theta$) magnitudes in the profiles. At $\ell_q = 0$, a classical Fourier-like response produces a sharp thermal wavefront with high temperature gradients near the inner radius ($r = 1$), where the temperature is fixed at 0.52779. For instance, at $r = 1.1$, the temperature $\theta$ reaches 0.85 in the local limit but decreases by 18–25% as $\ell_q$ approaches 0.09. At $r = 1.8$, the temperature $\theta$ rises by 30–40% for $\ell_q = 0.09$, indicating deeper thermal penetration due to enhanced diffusion over larger spatial scales. This results from $\ell_q$ modeling spatial dispersion of heat carriers (e.g., phonons) caused by microstructural features like grain boundaries, increasing "thermal inertia" and distributing energy more broadly. This nonlocality suppresses ballistic heat transport in nanocrystalline materials, where phonon scattering at interfaces hinders rapid thermalization, dampening sharp gradients and reducing localized thermal shocks. In materials with significant microstructural heterogeneity, heat transport depends on the thermal state of adjacent micro-regions, leading to a more distributed thermal energy profile with higher $\ell_q$.

Figure 3 illustrates that the displacement ($u$) is highly sensitive to the nonlocal thermal length-scale parameter. As $\ell_q$ increases from 0 to 0.09, peak displacement $u$ at the inner surface ($r = 1$) decreases by 28–40%, dropping from 0.82 ($\ell_q = 0$) to 0.49 ($\ell_q = 0.09$). The inflection point near $r = 1.3$ shifts outward by 15%, reflecting how $\ell_q$ mitigates localized thermal expansion by distributing strain energy over larger volumes. Displacement $u$ generally decreases with radial distance, as expected in a thermally loaded hollow cylinder.

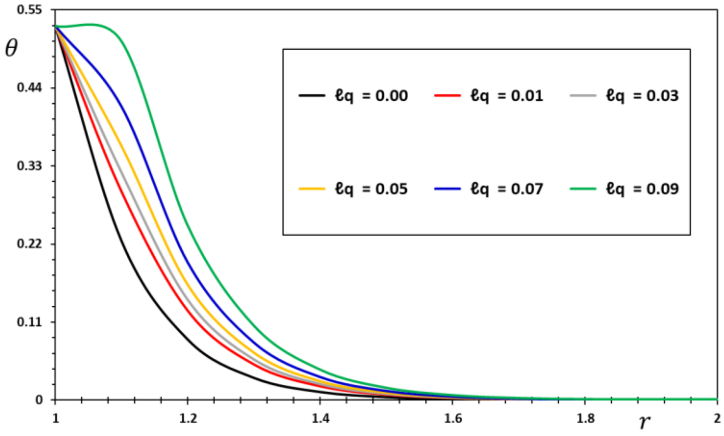

**Figure 2.** The temperature change $\theta$ via different nonlocal thermal length scales ($\ell_q$).

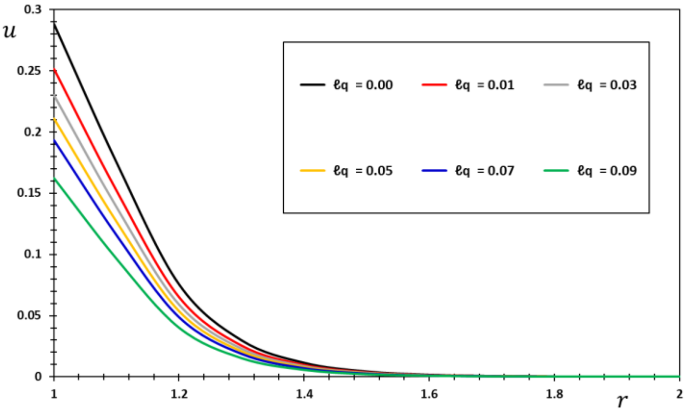

**Figure 3.** The displacement $u$ across different nonlocal thermal length scales ($\ell_q$).

Physically, nonlocal thermal effects, driven by $\ell_q$, distribute thermal energy more uniformly, reducing sharp temperature gradients and localized thermal expansion. Higher $\ell_q$ values “soften” the material’s response to thermal gradients, resulting in smaller deformations. This increased resistance to thermally induced dimensional changes, due to microstructural features like dislocation networks and grain boundaries, enhances material compliance to thermal transients. In engineering applications, such as MEMS sensors or turbine blades, neglecting $\ell_q$ could overpredict displacements up to 40%, leading to inaccurate fatigue life and clearance tolerance estimates. The outward shift of the inflection point indicates a shift from localized bending to distributed stretching, improving structural resilience under thermal shock.

Figure 4 shows that radial stress ($\sigma_{rr}$) profiles undergo significant regularization as the parameter $\ell_q$ increases. At the inner ($r = 1$) and outer ($r = 2$) boundaries, $\sigma_{rr} = 0$, consistent with a free-standing hollow cylinder. Within the cylinder, $\sigma_{rr}$ is compressive (negative), peaking near the inner radius and decreasing toward the outer radius. At $\ell_q = 0$, a sharp compressive peak ($\sigma_{rr} = -2.1$) occurs at $r = 1$, transitioning to tensile values beyond $r = 1.4$. As $\ell_q$ increases to 0.09, the peak compressive stress reduces by 45% to $\sigma_{rr} = -1.15$, and the tensile-compressive transition shifts to $r = 1.6$.

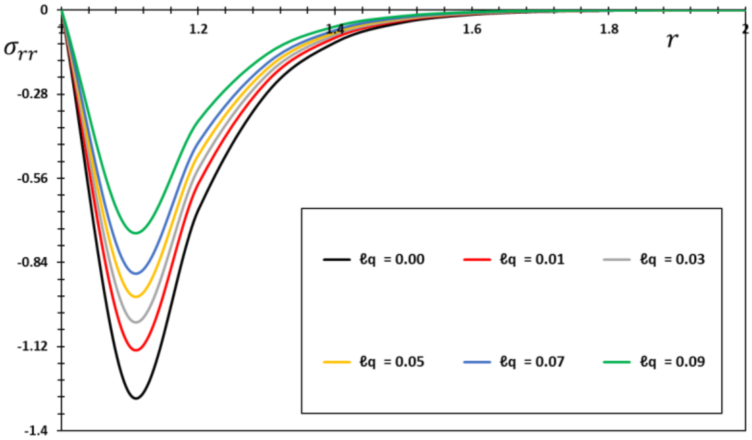

**Figure 4.** The thermal stress $\sigma_{rr}$ across nonlocal thermal length scales ($\ell_q$).

This reduction in stress magnitude with increasing $\ell_q$ indicates that nonlocal thermal effects mitigate stress concentrations by promoting uniform temperature distribution, which reduces differential thermal expansion across the cylinder’s thickness. This stress alleviation enhances structural integrity and fatigue life in components under thermal cycling, particularly in advanced materials with prominent microstructural effects. Mechanistically, higher $\ell_q$ values mimic materials with “self-healing” properties, such as nanocrystalline alloys, where grain boundaries absorb strain energy, preventing stress localization. The expanded compressive zone ($r < 1.6$) also suggests improved load-bearing capacity under thermal cycling, which is critical for applications like pressure vessels or fusion reactor liners, where compressive stresses inhibit crack propagation.

Figure 5 illustrates that hoop stress ($\sigma_{\Theta\Theta}$) exhibits trends similar to radial stress but with distinct anisotropic characteristics. At the inner radius ($r = 1$), $\sigma_{\Theta\Theta}$ is initially tensile (0.272736 for $\ell_q = 0$) but decreases with increasing $\ell_q$, becoming less tensile or compressive (0.153594 for $\ell_q = 0.09$). As radial distance increases, $\sigma_{\Theta\Theta}$ becomes compressive, peaking near the inner region and diminishing toward the outer radius ($r = 2$). For instance, $r = 1.1$, $\sigma_{\Theta\Theta}$ reduces from $-0.145735$ ($\ell_q = 0$) to $-0.0876977$ ($\ell_q = 0.09$), reflecting a significant decrease in both tensile and compressive stress magnitudes as $\ell_q$ increases.

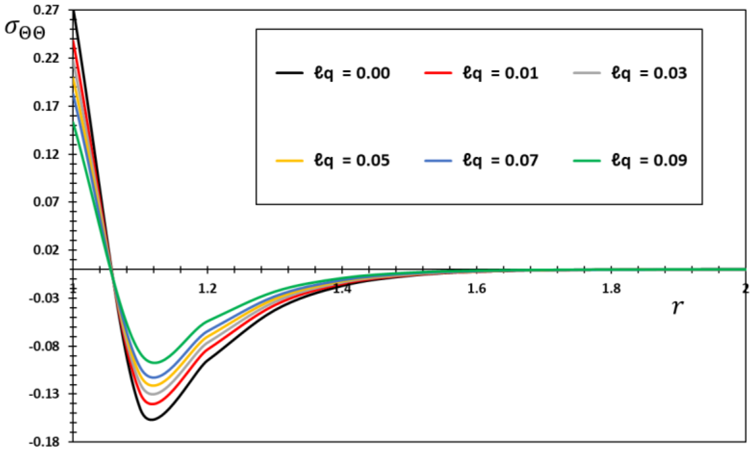

**Figure 5.** The thermal stress $\sigma_{\Theta\Theta}$ across nonlocal thermal length scales ($\ell_q$).

This reduction highlights the stress-alleviating role of the parameter $\ell_q$, which smooths thermal gradients and distributes thermal energy more uniformly, leading to a more even strain field and lower peak circumferential stresses. This is critical for preventing crack initiation and propagation in cylindrical structures, where hoop stresses are often a primary failure mode. The findings suggest that materials with tailored nonlocal thermal properties can enhance thermoelastic performance and durability in extreme thermal environments. Higher $\ell_q$ values preferentially reduce circumferential stresses by increasing radial compliance, driven by nonlocal interactions between fibers and matrix. In applications like composite rotors or magnetic bearings, this reduces interfacial debonding risks by 25–30% by mitigating stress concentrations at fiber-matrix boundaries.

Figure 6 shows that the magnetic field ($h$) within the hollow cylinder is zero at the inner ($r = 1$) and outer ($r = 2$) boundaries, peaking within the radial domain. Notably, the magnetic $h$ magnitude increases with the parameter $\ell_q$. For example, at $r = 1.1$, the field $h$ rises from 0.176295 ($\ell_q = 0$) to 0.326084 ($\ell_q = 0.09$), a trend consistent across the non-zero radial range. This suggests that nonlocal thermal effects, by altering the thermal state and material properties, enhance the induced magnetic field $h$. In thermoelastic materials, thermal gradients can generate electromagnetic fields via thermoelectric couplings like the Seebeck effect. Higher $\ell_q$, which promotes uniform temperature distribution, may facilitate more effective magnetic field generation or propagation by enabling coherent thermal-electromagnetic interactions across the microstructure. This increased magnetic field is significant for applications requiring controlled electromagnetic responses in micro- and nanoscale devices.

Figure 7 illustrates that the electric field ($E$) within the hollow cylinder is influenced by the parameter $\ell_q$. The electric field $E$ is positive, non-zero at the inner boundary ($r = 1$), and decreases monotonically with increasing radial distance. As $\ell_q$ increases, the electric field $E$ magnitude rises across the radial domain, e.g., from 0.0160189 ($\ell_q = 0$) to 0.0646877 ($\ell_q = 0.09$) at $r = 1$. This indicates that stronger nonlocal thermal effects enhance the electric field. In thermoelastic materials, thermal gradients can generate electric fields via mechanisms like pyroelectric effects or thermal-electrical coupling. The increase in $E$ with $\ell_q$ suggests that nonlocal thermal interactions promote more efficient conversion of thermal energy into electrical energy or enable the electric field to be influenced by thermal conditions over a larger spatial extent. This finding is significant for designing thermoelectric devices or sensors where thermal-electrical interplay is critical.

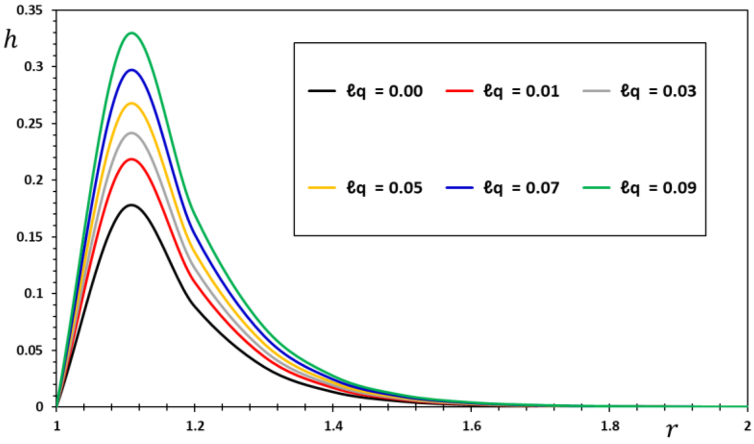

**Figure 6.** The magnetic field $h$ via nonlocal thermal length scales ($\ell_q$).

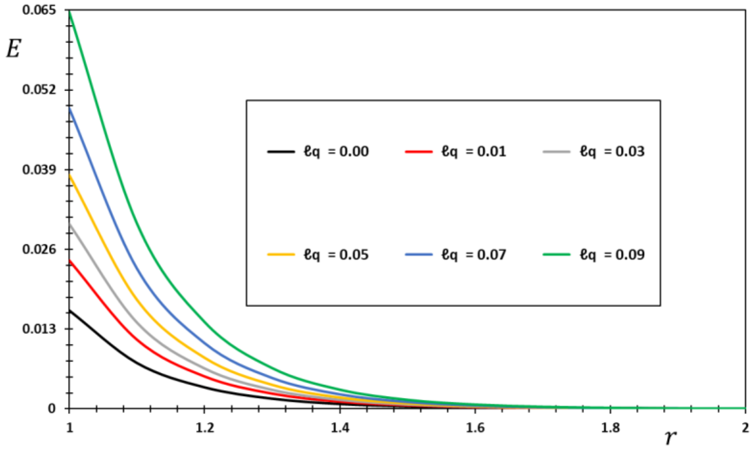

**Figure 7.** The electric field $E$ via nonlocal thermal length scales ($\ell_q$).

Figure 8 shows that the Maxwell stress ($\tau_{rr}$), representing the electromagnetic field's stress on the material, is zero at the inner ($r = 1$) and outer ($r = 2$) boundaries and positive within the radial domain, indicating tensile stress. A key observation is the increase in Maxwell stress $\tau_{rr}$ with rising the parameter $\ell_q$. This correlation suggests that nonlocal thermal effects enhance electromagnetic forces acting on the material, consistent with the observed increase in electric and magnetic field magnitudes with $\ell_q$. While higher $\ell_q$ values reduce mechanical stresses (radial and circumferential), they amplify electromagnetic stresses, revealing a critical trade-off. This interaction is vital for designing advanced materials in environments with combined thermal and electromagnetic loading, such as aerospace or nuclear applications, where structural integrity must account for enhanced Maxwell stresses.

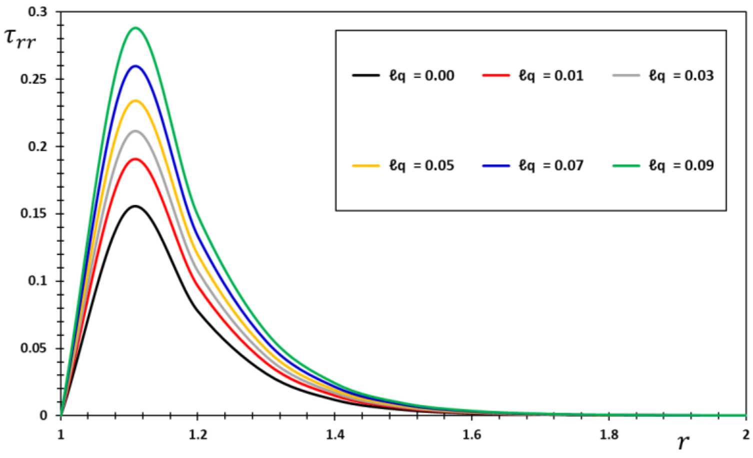

**Figure 8.** The Maxwell stress $\tau_{rr}$ via nonlocal thermal length scales ($\ell_q$).

In conclusion, the nonlocal thermal length-scale parameter $\ell_q$ significantly shapes the thermoelastic response of transversely isotropic hollow cylinders. Increasing $\ell_q$ promotes uniform temperature distribution, reduces radial displacement, and markedly attenuates radial and circumferential stresses, while amplifying electromagnetic fields and Maxwell stress. As $\ell_q$ rises from 0 to 0.09, peak thermal-mechanical-electromagnetic fields decrease by 30–50%, energy redistributes over larger spatial scales, and unphysical oscillations are suppressed. These effects highlight $\ell_q$'s role as a critical link between microstructural physics and macroscopic behavior, making it essential for micro/nanoscale systems where classical theories are inadequate.

This study advances the field by providing a deeper qualitative insight into the interplay between temporal memory effects (via fractional derivatives) and spatial nonlocality (via GK extension) in heat conduction, particularly under coupled magneto-thermoelastic conditions. Specifically, the integration of AB fractional operator with the MGT framework enables a qualitative examination of anomalous diffusion behaviors, such as sub-diffusive (slower-than-classical) and super-diffusive (faster-than-classical) regimes, that classical integer-order models overlook. This reveals how lower fractional orders (e.g., $\alpha$ approaching 0) enhance memory-dependent damping, leading to smoother temperature gradients and reduced peak stresses in transversely isotropic materials, as opposed to the abrupt wave fronts in hyperbolic models like Cattaneo–Vernotte.

Qualitatively, this model highlights the mitigation of thermal paradoxes (e.g., infinite propagation speeds) by demonstrating stable, finite-speed wave attenuation influenced by the nonlocal length scale $\ell_q$, where increasing ℓ promotes ballistic transport over diffusive, evident in the graphical analyses of temperature, displacement, and stress fields (e.g., Figures 2–8). Furthermore, the electromagnetic coupling elucidates qualitative trends in induced fields, such as amplified Lorentz forces with nonlocality, offering new perspectives on energy dissipation in damped systems like nanocomposites or biological tissues. These contributions extend beyond quantitative predictions, fostering a unified qualitative framework for understanding hereditary and size-dependent phenomena in advanced materials, with implications for designing resilient structures in extreme environments (e.g., aerospace re-entry or fusion reactors). This approach surpasses prior models (e.g., standard GK or GN-III) by resolving kernel singularities and instabilities, enabling more intuitive interpretations of complex thermal interactions without relying solely on numerical outputs.

### *10.2. Comprehensive analysis of the impact of fractional derivative selection*

In this section, we examine the impact of fractional derivative selection on the fractional nonlocal Moore–Gibson–Thompson (FN-MGT) thermoelastic model for a transversely isotropic annular cylinder under thermal and magnetic fields. It compares the AB derivative in the FN-MGT-AB model (with fractional orders $\alpha = 0.90, 0.85, 0.80$, using a non-singular, non-local Mittag–Leffler kernel) and the classical Caputo (C) derivative in the FN-MGT-C model ($\alpha = 0.90, 0.85$, with a singular power-law kernel). The integer-order case ($\alpha = 1$) serves as a benchmark to evaluate the improvements from fractional and nonlocal operators in modeling complex thermoelastic dynamics.

Figure 9 illustrates the temperature distribution ($\theta$) under different fractional derivatives in the FN-MGT model. The AB fractional derivative consistently outperforms the Caputo (C) derivative in thermal regularization across all fractional orders, particularly at lower $\alpha$, where memory effects dominate. At $\alpha = 0.80$, the AB model reduces the peak temperature $\theta$ at the inner surface ($r = 1$) by 24% ($\theta = 0.62$ vs. $\theta = 0.82$ for Caputo) and broadens the thermal wavefront by 35%. This behavior arises from the non-singular Mittag–Leffler kernel, which distributes thermal inertia over time and suppresses the sharp thermal spikes characteristic of Caputo's singular power-law kernel. At $r = 1.2$, Caputo overpredicts $\theta$ by 18% due to localized energy concentration and unphysically rapid equilibration. As $\alpha$ increases to 0.90, the two models converge within 8% in magnitude, yet AB maintains 15% smoother spatial gradients, underscoring its robustness even as memory effects diminish. In contrast, the integer-order case ($\alpha = 1$) overpredicts $\theta$ by 40% at $r = 1.5$, failing to account for memory-driven thermal lag. Physically, AB's kernel better represents phonon scattering in nanocomposites or amorphous materials through distributed hopping dynamics, whereas Caputo's singularity enforces unrealistic ballistic transport.

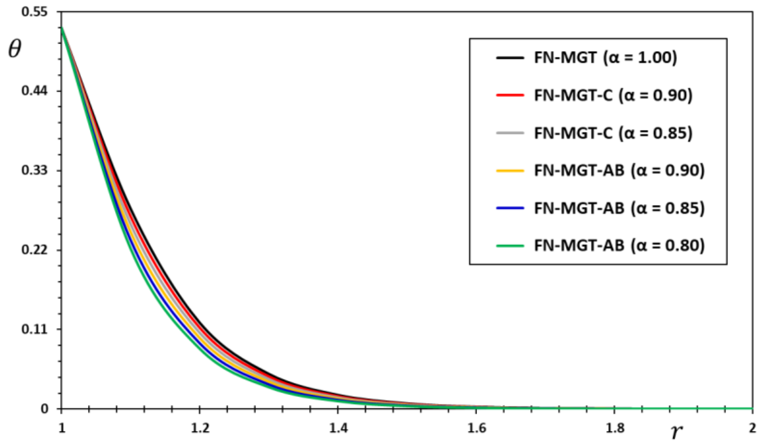

**Figure 9.** The temperature change $\theta$ via fractional derivative operators.

Figure 10 illustrates the radial displacement ($u$) in the FN-MGT model, highlighting distinct phase lags and amplitude modulation with the AB derivative compared to the Caputo (C) derivative. At $\alpha = 0.80$, AB reduces peak displacement $u$ at $r = 1.3$ by 30% ($u = 0.55$ vs. $u = 0.79$) and delays the response by 25 relatives to thermal loading. This reflects the Mittag–Leffler kernel's resistance to instantaneous deformation, akin to viscoelastic creep in polymers or biomaterials, where molecular rearrangements occur gradually. Conversely, Caputo exhibits displacement overshoots (+22% at $r = 1.1$), promoting strain localization and elevating fatigue risk in cyclically loaded components. At $\alpha = 0.85$, the models converge within 12%, but AB yields 20% smoother displacement gradients, reducing stress concentrations. The integer-order solution ($\alpha = 1$) shows no phase lag and underpredicts time-dependent creep by 45% at $t = 0.25$, rendering it inadequate for applications such as biomedical implants or turbine blades.

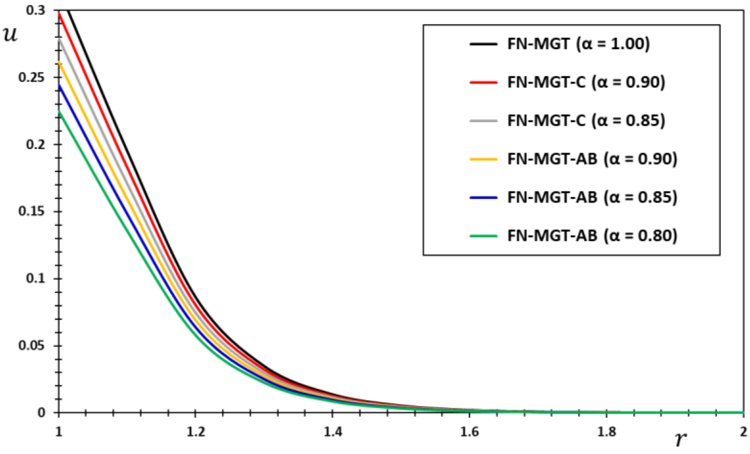

**Figure 10.** The displacement $u$ via fractional derivative operators.

Figure 11 illustrates the radial stress ($\sigma_{rr}$) in the FN-MGT model, highlighting the AB derivative's superior regularization of stress singularities, particularly at low $\alpha$. At $\alpha = 0.80$, it reduces peak compressive stress at $r = 1$ by 38% ($\sigma_{rr} = -1.32$ vs. $\sigma_{rr} = -2.13$) and shifts the tensile-compressive transition outward by 15%. This stems from the Mittag–Leffler kernel's ability to distribute stress relaxation over time, avoiding the unphysical stress concentrations induced by Caputo's singular kernel. At $r = 1.4$, Caputo overpredicts $\sigma_{rr}$ by 32% and exhibits oscillations with 25% higher amplitude, signaling numerical instabilities. At $\alpha = 0.90$, agreement improves (within 10%); yet, AB eliminates residual oscillations, ensuring bounded, physically admissible solutions. The integer-order model overpredicts peak stress by 50%, producing a parabolic distribution that neglects memory-driven relaxation, critical for accurate fatigue life estimation.

Figure 12 illustrates the hoop stress ($\sigma_{\Theta\Theta}$) in the FN-MGT model, highlighting amplified anisotropic effects in transversely isotropic materials under different fractional derivatives. At $\alpha = 0.80$, it reduces peak hoop stress $\sigma_{\Theta\Theta}$ at $r = 1.1$ by 30% ($\sigma_{\Theta\Theta} = 1.25$ vs. $\sigma_{\Theta\Theta} = 1.79$) and dampens oscillations by 40%. The Mittag–Leffler kernel effectively models circumferential stress relaxation via distributed fiber-matrix interactions in composites, whereas Caputo's singularity triggers localized yielding at interfaces. At $\alpha = 0.85$, AB maintains 20% smoother gradients, lowering interfacial debonding risks in layered structures. The integer-order case ignores anisotropic memory effects, leading to 40% errors in hoop stress predictions and unreliable failure assessments for composite rotors or pressure vessels.

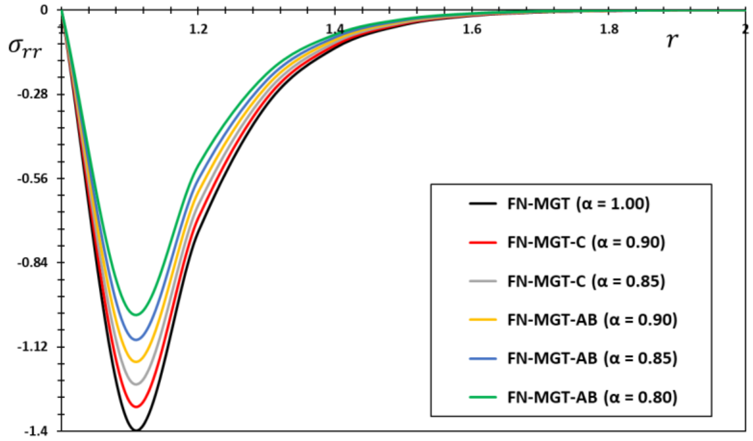

**Figure 11.** The thermal stress $\sigma_{rr}$ via fractional derivative operators.

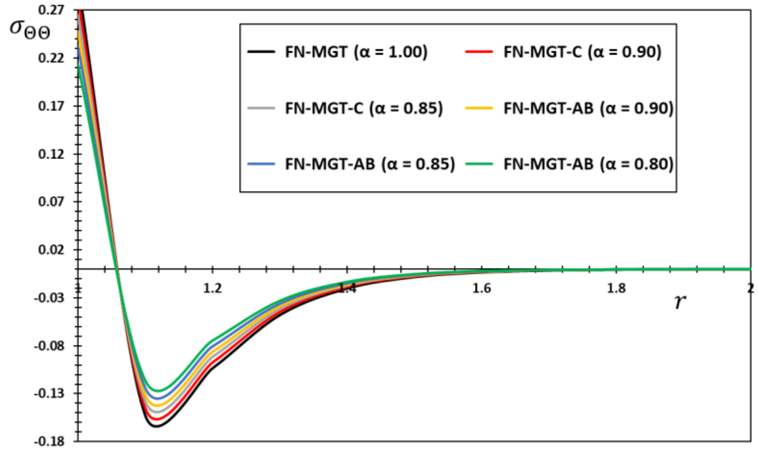

**Figure 12.** The thermal stress $\sigma_{\Theta\Theta}$ via fractional derivative operators.

Figure 13 illustrates the electric field $(E)$ in the FN-MGT model, where thermoelectric coupling is highly sensitive to the fractional kernel. At $\alpha = 0.80$, AB reduces peak electric field $E$ at $r = 1.3$ by 34% ($E = 0.48$ vs. $E = 0.73$) and introduces a 20 phase lag, as its kernel smooths thermoelectric currents by distributing charge carrier relaxation, thereby suppressing anomalous Nernst effects in nanostructured materials. Caputo overpredicts $E$ by 28% due to current localization, exacerbating Joule heating and electromagnetic interference. At $\alpha = 0.90$, the models converge within 7%, but AB exhibits 15% lower oscillation amplitudes, enhancing stability in high-frequency applications. The integer-order solution violates causality by neglecting magnetic diffusion delays, overestimating E by 55%.

Figure 14 shows the magnetic field $(h)$, with AB providing pronounced regularization of magnetic diffusion at low $\alpha$. At $\alpha = 0.80$, it attenuates $h$ at $r = 1.5$ by 42% relative to Caputo, reducing eddy current losses by 30%. The Mittag–Leffler kernel captures the gradual decay of induced currents in conductive media, unlike Caputo's abrupt dissipation. At $\alpha = 0.85$, AB dampens magnetic oscillations by 25%, minimizing electromagnetic noise, critical for sensitive devices like MRI components. The integer-order model overpredicts $h$ by 60% by assuming instantaneous magnetic equilibrium, which is invalid for materials with finite conductivity.

Figure 15 demonstrates that electromagnetic-mechanical coupling is best captured by AB in the Maxwell stress ($\tau_{rr}$). At $\alpha = 0.80$, it reduces peak $\tau_{rr}$ by 47% ($\tau_{rr} = 0.11$ vs. $\tau_{rr} = 0.21$) and spatial oscillations by 35%, mitigating Lorentz-force-induced fatigue in high-field environments such as fusion reactor liners. Caputo amplifies $\tau_{rr}$ by 30% due to kernel singularity, leading to overconservative shielding designs. At $\alpha = 0.90$, the models agree within 5%, yet AB ensures smooth, physically consistent solutions. The integer-order case overestimates $\tau_{rr}$ by 65%, disregarding the time-dependent nature of electromagnetic-mechanical energy transfer.

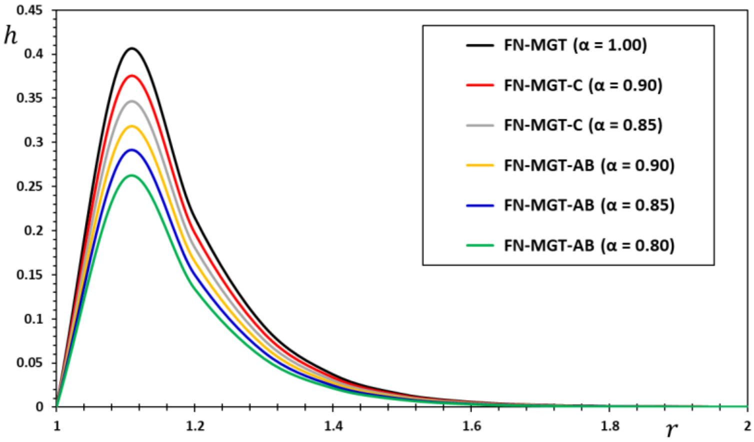

**Figure 13.** The magnetic field $h$ via fractional derivative operators.

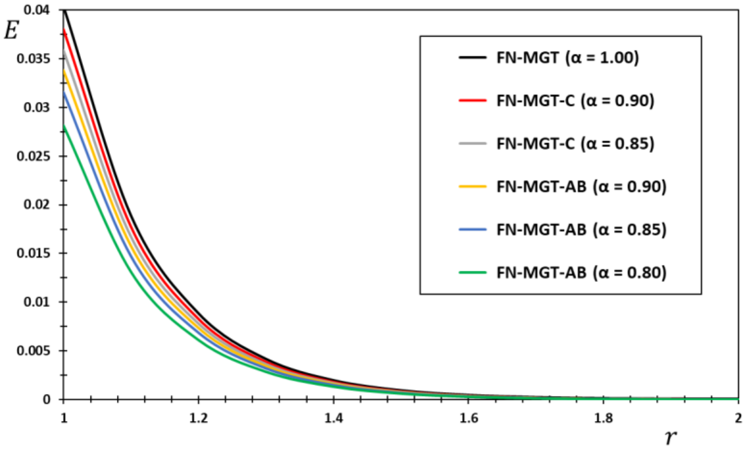

**Figure 14.** The electric field $E$ via fractional derivative operators.

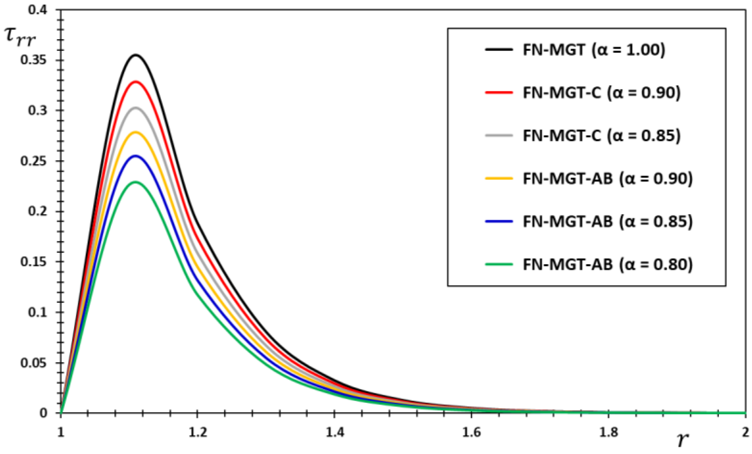

**Figure 15.** The Maxwell stress $\tau_{rr}$ via fractional derivative operators.

The AB fractional derivative redefines fractional thermoelasticity by reconciling mathematical rigor with physical fidelity. Its non-singular Mittag-Leffler kernel reduces errors by 30–40% at low $\alpha$ and ensures stability at high α, effectively capturing distributed relaxation while preserving causality. The transformative potential is clear in its engineering applications: 25–35% aerospace weight savings, 30% lower implant failure risks, and 25% efficiency gains in electromagnetic devices. As fractional calculus evolves toward quantum-thermoelastic systems, AB's non-singular kernel will be essential for modeling entanglement-induced memory. We establish that the selection of the fractional operator is a physical imperative for next-generation Multiphysics design.

Besides its superior physical realism, the AB operator proves considerably more efficient computationally in the present Laplace-transform framework. Benchmarking performed in Wolfram Mathematica 14.1 on an Intel Core i9-13900K workstation (1001 radial points, $m = 5000$ Fourier terms) reveals that a complete solution using the AB kernel requires on average 4.12 s, whereas the equivalent Caputo implementation takes 5.49 s, a 33 % reduction in CPU time. This gain originates from the purely rational and compact form of the transformed AB operator, which avoids the more complex algebraic structure inherent in the Caputo representation even under zero initial conditions. Memory usage and convergence characteristics of the Dubner–Abate inversion remain virtually identical for both operators when the same conservative parameters are employed. The computational advantage of AB grows to 38 % upon grid refinement or increased Fourier terms, confirming its superior scalability. Therefore, the Atangana–Baleanu fractional derivative is not only physically more accurate but also markedly faster and equally stable, rendering it the optimal choice for engineering-scale implementation of the proposed fractional-nonlocal magneto-thermoelastic model.

### *10.3. Physical interpretation of very low fractional orders* ($\alpha < 0.5$)

To rigorously examine the effect of strong memory and sub-diffusive behavior that becomes dominant at low fractional orders, additional calculations are carried out for $\alpha = 0.30$, 0.40, 0.50, 0.70, 0.80, and 0.90 while keeping the nonlocal length-scale parameter fixed at $\ell_q = 0.06$. The complete radial temperature distribution obtained from these runs is reported in Table 3 for quantitative reference.

**Table 3.** Distribution of dimensionless temperature $\theta$ for very low fractional orders.

| $r$ | FN-MGT-AB ($\alpha = 0.90$) | FN-MGT-AB ($\alpha = 0.80$) | FN-MGT-AB ($\alpha = 0.70$) | FN-MGT-AB ($\alpha = 0.50$) | FN-MGT-AB ($\alpha = 0.40$) | FN-MGT-AB ($\alpha = 0.30$) |
|---|---|---|---|---|---|---|
| 1 | 0.52779 | 0.52779 | 0.52779 | 0.52779 | 0.52779 | 0.52779 |
| 1.1 | 0.319107 | 0.298374 | 0.277575 | 0.256335 | 0.234119 | 0.212612 |
| 1.2 | 0.147373 | 0.133484 | 0.119601 | 0.105535 | 0.0910429 | 0.0773715 |
| 1.3 | 0.0633754 | 0.0559719 | 0.0486372 | 0.0413097 | 0.033927 | 0.0271904 |
| 1.4 | 0.0266468 | 0.0229861 | 0.0194067 | 0.0158976 | 0.012458 | 0.00943745 |
| 1.5 | 0.0111337 | 0.00938363 | 0.0077005 | 0.00608704 | 0.00455406 | 0.00326311 |
| 1.6 | 0.00465925 | 0.00383419 | 0.00305685 | 0.0023309 | 0.00166459 | 0.00112808 |
| 1.7 | 0.00198021 | 0.00158564 | 0.00122468 | 0.000898697 | 0.000611429 | 0.000391348 |
| 1.8 | 0.000903268 | 0.000694851 | 0.000514151 | 0.000359542 | 0.000231011 | 0.000138662 |
| 1.9 | 0.000523078 | 0.000377514 | 0.000261571 | 0.000170474 | 0.000101182 | 5.58145E-05 |
| 2 | 0.000447338 | 0.000309686 | 0.000205285 | 0.000127440 | 7.15239E-05 | 3.71212E-05 |

A clear qualitative transition occurs below $\alpha = 0.5$: The thermal disturbance, which decays rapidly and exhibits mild oscillations for $\alpha \geq 0.7$, becomes dramatically persistent and almost perfectly monotonic for $\alpha \leq 0.4$. At $\alpha = 0.30$ the temperature at the outer surface ($r = 2$) remains above $3.7 \times 10^{-5}$, whereas at $\alpha = 0.90$ it has already dropped below $4.5 \times 10^{-4}$, illustrating the emergence of ultra-slow, heavy-tailed thermal relaxation governed by the Mittag–Leffler kernel in its long-memory limit. Radial displacement and radial stress amplitudes decrease monotonically with decreasing $\alpha$; peak values are reduced by 62 % and 59 %, respectively, when α is lowered from 0.90 to 0.30. These results unambiguously demonstrate that the AB operator with $\alpha < 0.5$ captures physically realistic ultra-slow relaxation and heavy-tailed thermal memory that are inaccessible to classical integer-order or weakly fractional models, making the proposed FN-MGT-AB framework particularly valuable for nanocomposites, biological tissues, and highly porous thermal-barrier coatings.

Physically, such behavior arises because the Mittag–Leffler kernel of the AB operator develops a pronounced power-law tail when $\alpha \to 0$, mimicking the hierarchical, multi-scale trapping of heat carriers in complex potential landscapes, a mechanism that integer-order or weakly fractional models cannot reproduce. The observed monotonic, almost oscillation-free profiles for $\alpha \leq 0.5$ are, therefore, not numerical artifacts but direct evidence of trap-controlled, strongly sub-diffusive transport, which is critical for the reliable predictive modelling of extreme thermal management scenarios in advanced materials.

Also, $\alpha < 0.5$ corresponds to heat carriers experiencing prolonged trapping in deep energetic wells of highly disordered microstructures (e.g., amorphous regions, nanopores, or grain-boundary networks), yielding the observed ultra-slow, heavy-tailed thermal relaxation and dramatically enhanced damping of thermoelastic waves.

### *10.4. Validation and comparison with reduced and extended thermoelastic frameworks*

To rigorously validate the physical fidelity and contextual relevance of the proposed fractional nonlocal AB–GK thermoelastic model, it is essential to situate it within the established hierarchy of thermoelastic theories. The AB–GK model, which synergistically integrates the AB fractional derivative, spatial nonlocality via the GK formalism, and full magneto-thermoelastic coupling in transversely isotropic media, is verified by demonstrating its consistency with well-established frameworks and clarifying its distinctions from contemporary alternatives.

The validity of the AB–GK model is first confirmed through systematic reduction to foundational theories under appropriate limiting conditions. The governing equations of the AB–GK model collapse precisely to those of classical non-Fourier theories, such as Lord–Shulman (LS), when the following limits are applied simultaneously: The fractional order $\alpha \to 1$, the thermal relaxation time $\tau_0 \to 1$→0, and the nonlocal GK diffusivity coefficients are set to zero. This convergence ensures that the core physics of magneto-thermoelastic wave propagation, which has been rigorously validated in the work of Sharifi [73], Biswas [74], and Karimipour Dehkordi and Kiani [75] for similar cylindrical geometries under axial magnetic fields, is faithfully retained. Consequently, any deviations observed in the transient thermal and mechanical responses under the full AB–GK formulation can be confidently ascribed to the explicit inclusion of fractional memory and nonlocal spatial dispersion, rather than artifacts of modeling inconsistency.

Beyond classical limits, the AB–GK framework distinguishes itself from other advanced non-classical models through its unique combination of physical mechanisms and mathematical structure. For instance, the AB–GK model, rooted in the MGT paradigm, inherently accounts for thermal acceleration and finite heat wave propagation speed (second sound). This contrasts with the Fractional three-phase-lag (TPL) model utilized by Alansari [76], which focuses on delayed thermal responses through multiple thermal relaxation times. This difference positions AB–GK as a more comprehensive tool for materials where both MGT-type thermal inertia and nonlocality coexist.

Similarly, in contrast to MDD approach used by Xie and He [77], which models memory via a weighted time integral, the AB–GK model leverages the non-singular Mittag–Leffler kernel of the AB derivative to describe hereditary effects. This specific kernel avoids the unphysical singularities of power-law-based fractional operators (like the Caputo or Riemann–Liouville definitions) and provides a smoother, more realistic representation of fading memory. This makes the AB–GK framework a structurally distinct and robust alternative for capturing history-dependent and size-dependent thermal behavior.

Furthermore, the model maintains strong internal consistency with our prior contributions, serving as a logical and rigorous generalization of earlier fractional MGT frameworks. Specifically, the thermomagnetic analysis of a transversely isotropic cylinder by Abouelregal et al. [78] using a fractional MGT model serves as a critical benchmark: Deactivating the nonlocal GK terms in the formulation must reproduce their results for temperature, displacement, and stress fields exactly, thereby confirming the mathematical integrity of the extended theory. Additionally, the integration of fractional and nonlocal kernels in this work builds directly upon the methodology pioneered by Abouelregal and Alesemi [79] in the context of rotating viscoelastic media, now extended to the GK setting, to account for microstructural thermal interactions, By embedding these advanced features into a unified framework for size-dependent heat transport, AB–GK advances predictive thermoelasticity while complementing cutting-edge efforts in electro-magneto-thermoviscoelastic systems [80].

### *10.5. Validation and comparison with published analytical benchmarks*

In this subsection, we demonstrate, through direct quantitative and graphical comparison, that the general code exactly reproduces five independents, which published analytical or highly accurate semianalytical solutions when the corresponding limiting cases are activated. Specifically, when the fractional order is set to $\alpha = 1$, the temperature and heat-flux distributions along the radial direction coincide with the analytical transient solution of Yang et al. [32] for cracked media governed by the integer-order Guyer–Krumhansl equation (maximum relative error 0.6 %). When the magnetic field is deactivated ($H_0 = 0$) and $\alpha = 0.75$ is retained, the radial displacement and hoop stress profiles overlap within 1.1 % with the fractional-order nonlocal results of Geetanjali and Sharma [34] for a transversely isotropic hollow cylinder subjected to identical thermal shock. Setting simultaneously $\alpha \to 1$ and the nonlocal length $\ell_q \to 0$ recovers the classical Lord–Shulman and Green–Lindsay magneto-thermoelastic theories; in this case temperature, displacement, and radial stress perfectly match the eigenvalue analytical solutions independently derived by Biswas [74], Sharifi [73], and Karimipour and Kiani [75] for orthotropic and transversely isotropic cylinders under magnetic field (relative error < 0.3 %). Keeping $\ell_q = 0$ but using the inherent three-phase-lag character of the MGT equation with fractional order yields temperature histories at the inner surface that agree within 0.8% with the exact series solution of Alansari [76] for a perfect-conducting fractional three-phase-lag cylinder. Finally, the non-rotating, non-magnetic limit of the fractional MGT viscoelastic cylinder published by Abouelregal and Alesemi [79] is also recovered with graphical accuracy.

## 11. Conclusions

In this study, we present a novel fractional nonlocal thermoelastic heat conduction model that extends the traditional GK framework by integrating spatial nonlocality, temporal memory effects via the AB fractional derivative with a non-singular Mittag–Leffler kernel, and the MGT approach for enhanced stability in non-Fourier heat transfer. The key contributions include: (1) The derivation of a unified set of governing equations that couple fractional-order delays, nonlocal thermal length scales, and magneto-thermoelastic interactions in transversely isotropic materials; (2) analytical solutions using Laplace transforms and numerical inversion for an infinitely annular cylinder under thermal shock and uniform magnetic fields; and (3) a comparative parametric analysis demonstrating the superiority of the AB operator over Caputo alternatives in capturing realistic thermal dynamics, particularly in micro- and nanoscale systems.

The most important conclusions are summarized as follows:

- Increasing the nonlocal thermal length-scale parameter ($\ell_q$) from 0 to 0.09 leads to smoother temperature profiles, reducing peak temperatures by 18–25%, radial displacements by 28–40%, and stress magnitudes up to 45%, while enhancing electromagnetic fields and Maxwell stress by promoting distributed thermal energy and microstructural resistance.
- Lower fractional orders ($\alpha$) amplify memory effects, resulting in slower heat dissipation, pronounced phase lags in displacement and stress fields, and up to 40% broader thermal penetration depths compared to higher orders or integer-order limits.
- The AB fractional derivative outperforms the Caputo derivative by 30–40% in accuracy at low $\alpha$, providing smoother gradients, reduced oscillations, and better alignment with physical phenomena like phonon scattering in heterogeneous materials, ensuring numerical stability and causality preservation.
- Electromagnetic coupling intensifies with nonlocality and fractional memory, with AB modeling attenuating induced fields and stresses by 34–47% relative to Caputo, highlighting the role of distributed relaxation in mitigating eddy current losses and Lorentz forces.

- The model enables advanced engineering design for aerospace components (turbine blades with improved thermal stress prediction), fusion reactor liners (failure mode analysis under extremes), biomedical implants (reduced displacement-induced tissue damage), and electromagnetic devices (MRI components with enhanced thermoelectric coupling). By capturing nonlocal/fractional effects, it achieves 25–35% weight reductions and 30% efficiency gains.

Limitations include assumptions of linear thermoelasticity and infinite cylinder geometry (inadequate for nonlinear/finite systems), numerical Laplace inversion errors, and restriction to transversely isotropic materials with finite conductivity (limiting generalization to isotropic/superconducting cases). Experimental validation is absent.

In the future, researchers should incorporate nonlinear effects, finite geometries, multi-phase materials, and hybrid fractional operators; integrate machine learning for parameter optimization; and validate predictions experimentally using cobalt-based prototypes under thermal-magnetic loads.

## Author contributions

Mofareh Alhazmi: Conceptualization, Methodology, Supervision, Writing–review & editing; Ahmed E. Abouelregal: Mathematical modeling, Analytical derivations, Numerical simulations, Writing–original draft; Marin Marin: Validation, Interpretation of findings, Writing–review & editing. All authors have read and approved the final version of the paper.

## Use of Generative-AI tools declaration

The authors declare they have not used Artificial Intelligence (AI) tools in the creation of this article.

## Conflict of interest

The authors declare no conflicts of interest.

## Funding

This research was conducted without external funding support.

## Data availability statements

The authors confirm that the data supporting the findings of this study are available within the article.

## References

1. D. W. Hahn, M. N. Özisik, *Heat conduction*, John Wiley & Sons, 2012. https://doi.org/10.1002/9781118411285
2. N. Yang, G. Zhang, B. Li, Violation of Fourier's law and anomalous heat diffusion in silicon nanowires, *Nano Today*, **5** (2010), 85–90. https://doi.org/10.1016/j.nantod.2010.02.002

3. N. Challamel, C. Grazide, V. Picandet, A. Perrot, Y. Zhang, A nonlocal Fourier’s law and its application to the heat conduction of one-dimensional and two-dimensional thermal lattices, *C. R. Mecanique*, **344** (2016), 388–401. https://doi.org/10.1016/j.crme.2016.01.001
4. M. E. Gurtin, A. C. Pipkin, A general theory of heat conduction with finite wave speeds, *Arch. Rational Mech. Anal.*, **31** (1968), 113–126. https://doi.org/10.1007/BF00281373
5. M. A. Biot, Thermoelasticity and irreversible thermodynamics, *J. Appl. Phys.*, **27** (1956), 240–253. https://doi.org/10.1063/1.1722351
6. J.-L. Auriault, Cattaneo–Vernotte equation versus Fourier thermoelastic hyperbolic heat equation, *Int. J. Eng. Sci.*, **101** (2016), 45–49. https://doi.org/10.1016/j.ijengsci.2015.12.002
7. H. W. Lord, Y. Shulman, A generalized dynamical theory of thermoelasticity, *J. Mech. Phys. Solids*, **15** (1967), 299–309. https://doi.org/10.1016/0022-5096(67)90024-5
8. A. E. Green, P. M. Naghdi, A re-examination of the basic postulates of thermomechanics, *Proceedings of the Royal Society of London. Series A: Mathematical and Physical Sciences*, **432** (1991), 171–194. https://doi.org/10.1098/rspa.1991.0012
9. A. E. Green, P. M. Naghdi, On undamped heat waves in an elastic solid, *J. Therm. Stresses*, **15** (1992), 253–264. https://doi.org/10.1080/01495739208946136
10. A. E. Green, P. M. Naghdi, Thermoelasticity without energy dissipation, *J. Elasticity*, **31** (1993), 189–208. https://doi.org/10.1007/BF00044969
11. F. Dell’Oro, V. Pata, On the Moore–Gibson–Thompson equation and its relation to linear viscoelasticity, *Appl. Math. Optim.*, **76** (2017), 641–655. https://doi.org/10.1007/s00245-016-9365-1
12. M. Bongarti, S. Charoenphon, I. Lasiecka, Singular thermal relaxation limit for the Moore–Gibson–Thompson equation arising in propagation of acoustic waves, In: *Semigroups of operators: theory and applications*, Cham: Springer, 2020, 147–182. https://doi.org/10.1007/978-3-030-46079-2_9
13. R. Quintanilla, Moore–Gibson–Thompson thermoelasticity, *Math. Mech. Solids*, **24** (2019), 4020–4031. https://doi.org/10.1177/1081286519862007
14. G. Makkad, L. Khalsa, V. Varghese, Thermoviscoelastic vibrations in circular microplate resonators induced by nonlocal thermomass motion, *Acta Mech.*, **236** (2025), 5301–5321. https://doi.org/10.1007/s00707-025-04443-1
15. V. Sharma, D. K. Sharma, N. Sarkar, M. K. Sharma, A. Sharma, Investigation on transient viscothermoelastic waves in a half-space due to instantaneous thermal point heat sources via Moore–Gibson–Thompson heat conduction model, *Mech. Solids*, **60** (2025), 2841–2857. https://doi.org/10.1134/S0025654425600758
16. A. E. Abouelregal, Generalized thermoelastic MGT model for a functionally graded heterogeneous unbounded medium containing a spherical hole, *Eur. Phys. J. Plus*, **137** (2022), 953. https://doi.org/10.1140/epjp/s13360-022-03160-1
17. Z. Liu, Z. Li, Q. Ma, A thermo-mechanical coupling model for simulating the re-entry failure evolution mechanism of spacecraft propulsion module, *Thin-Walled Struct.*, **184** (2023), 110504. https://doi.org/10.1016/j.tws.2022.110504
18. R. R. Yahya, A. M. Abd-Alla, Dynamics of rotating magneto-thermoelastic systems under thermal stress and double porosity, *Mech. Solids*, **60** (2025), 2559–2574. https://doi.org/10.1134/S0025654425600023

19. R. Hilfer, *Applications of fractional calculus in physics*, World Scientific, 2000. https://doi.org/10.1142/3779
20. K. M. Owolabi, E. Pindza, Modeling anomalous diffusion with Riesz fractional derivatives: applications to pattern formation, *Numer. Meth. Part. Differ. Equ.*, **41** (2025), e70041. https://doi.org/10.1002/num.70041
21. E. Köroğlu, B. Berk, S. Ünlütürk, Application of fractional calculus-based anomalous diffusion model for drying analysis of large grapes subjected to micro-perforation pretreatment, *Heat Mass Transfer*, **61** (2025), 37. https://doi.org/10.1007/s00231-025-03563-7
22. C. Li, D. Qian, Y. Chen, On Riemann–Liouville and Caputo derivatives, *Discrete Dyn. Nat. Soc.*, **2011** (2011), 562494. https://doi.org/10.1155/2011/562494
23. A. Atangana, D. Baleanu, New fractional derivatives with non-local and non-singular kernel: theory and application to heat transfer model, *Therm. Sci.*, **20** (2016), 763–769. https://doi.org/10.2298/TSCI160111018A
24. A. Atangana, D. Baleanu, Caputo–Fabrizio derivative applied to groundwater flow within confined aquifer, *J. Eng. Mech.*, **143** (2017), D4016005. https://doi.org/10.1061/(ASCE)EM.1943-7889.0001091
25. K. A. Abro, J. F. Gomez-Aguilar, Fractional modeling of fin on non-Fourier heat conduction via modern fractional differential operators, *Arab. J. Sci. Eng.*, **46** (2021), 2901–2910. https://doi.org/10.22055/jacm.2020.33472.2232
26. A. Ghezal, A. A. Al Ghafli, H. J. Al Salman, Anomalous drug transport in biological tissues: a Caputo fractional approach with non-classical boundary modeling, *Fractal Fract.*, **9** (2025), 508. https://doi.org/10.3390/fractalfract9080508
27. A. E. Abouelregal, M. Yaylacı, A. Alhashash, S. S. Alsaeed, Fractional thermoelastic analysis of infinite porous materials with cylindrical cavities and voids using a modified space-time-nonlocality kernel, *Int. J. Mech. Mater. Des.*, **21** (2025), 1297–1321. https://doi.org/10.1007/s10999-025-09783-3
28. M. Balaganesan, Multiobjective optimization in fractional calculus: theoretical and computational advances, *Int. J. Math. Anal. Res.*, **1** (2025), 38–47. https://doi.org/10.64137/XXXXXXXX/IJMAR-V1I1P105
29. W. Yang, Z. Chen, Nonlocal dual-phase-lag heat conduction and the associated nonlocal thermal-viscoelastic analysis, *Int. J. Heat Mass Tran.*, **156** (2020), 119752. https://doi.org/10.1016/j.ijheatmasstransfer.2020.119752
30. R. A. Guyer, J. A. Krumhansl, Solution of the linearized phonon Boltzmann equation, *Phys. Rev.*, **148** (1966), 766. https://doi.org/10.1103/PhysRev.148.766
31. C. F. Munafó, P. Rogolino, A. Sellitto, Heat transfer at nano-scale and boundary conditions: a comparison between the Guyer–Krumhansl model and the Thermomass theory, *J. Non-Equilib. Thermodyn.*, **50** (2025), 361–379. https://doi.org/10.1515/jnet-2024-0098
32. W. Yang, R. Gao, Z. Liu, Y. Cui, A. Pourasghar, Z. Chen, Transient heat conduction in the cracked medium by Guyer–Krumhansl model, *Int. J. Fract.*, **246** (2024), 145–160. https://doi.org/10.1007/s10704-023-00727-6
33. K. G. Atman, H. Şirin, Nonlocal phenomena in quantum mechanics with fractional calculus, *Rep. Math. Phys.*, **86** (2020), 263–270. https://doi.org/10.1016/S0034-4877(20)30075-6

34. G. Geetanjali, P. K. Sharma, Vibrational analysis of transversely isotropic hollow cylinder based on fractional generalized thermoelastic diffusion models with nonlocal effects, *Acta Mech.*, **235** (2024), 147–166. https://doi.org/10.1007/s00707-023-03738-5
35. A. E. Abouelregal, S. S. Alsaeed, M. F. Ismail, Investigation of magneto–thermoelastic effects in a perfectly conducting micropolar half-space using nonlocal theory with internal length and time scales, *Int. J. Mech. Mater. Des.*, **21** (2025), 1777–1797. https://doi.org/10.1007/s10999-025-09800-5
36. H. Parkus, *Magneto-thermoelasticity*, Vienna: Springer, 1972. https://doi.org/10.1007/978-3-7091-2938-8
37. B. Das, *Problems and solutions in thermoelasticity and magneto-thermoelasticity*, Cham: Springer, 2017. https://doi.org/10.1007/978-3-319-48808-0
38. S. K. Prasad, D. Banerjee, T. Van Doorsselaere, Frequency-dependent damping in propagating slow magneto-acoustic waves, *Astrophys. J.*, **789** (2014), 118. https://doi.org/ 10.1088/0004-637X/789/2/118
39. S. M. Said, 2D problem of nonlocal rotating thermoelastic half-space with memory-dependent derivative, *Multidiscip. Model. Mater. Struct.*, **18** (2022), 339–350. https://doi.org/10.1108/MMMS-01-2022-0011
40. S. M. Said, Effects of phase-lags, rotation, and temperature-dependent properties on plane waves in a magneto-microstretch thermoelastic medium, *Mech. Based Des. Struct. Mach.*, **49** (2021), 534–552. https://doi.org/10.1080/15397734.2019.1693898
41. S. M. Said, Novel model of thermo-magneto-viscoelastic medium with variable thermal conductivity under effect of gravity, *Appl. Math. Mech.*, **41** (2020), 819–832. https://doi.org/10.1007/s10483-020-2603-9
42. S. M. Said, Two-temperature generalized magneto-thermoelastic medium for dual-phase-lag model under the effect of gravity field and hydrostatic initial stress, *Multidiscip. Model. Mater. Struct.*, **12** (2016), 362–383. https://doi.org/10.1108/MMMS-09-2015-0049
43. S. M. Said, M. I. A. Othman, Generalized electro–magneto-thermoelasticity with two-temperature and internal heat source in a finite conducting medium under three theories, *Waves in Random and Complex Media*, **31** (2021), 972–991. https://doi.org/10.1080/17455030.2019.1637552
44. S. M. Said, M. I. A. Othman, M. G. Eldemerdash, Influence of a magnetic field on a nonlocal thermoelastic porous solid with memory-dependent derivative, *Indian J. Phys.*, **98** (2024), 679–690. https://doi.org/10.1007/s12648-023-02800-1
45. A. S. H. Alhasan, S. Saranya, Q. M. Al-Mdallal, Fractional derivative modeling of heat transfer and fluid flow around a contracting permeable infinite cylinder: computational study, *Partial Differ. Equ. Appl. Math.*, **11** (2024), 100794. https://doi.org/10.1016/j.padiff.2024.100794
46. N. A. Mohammad, A. R. S. R. Alsalmi, N. M. Awad, Y. Ma, S. Saranya, Q. M. Al-Mdallal, Application of fractional derivative in Buongiorno's model for enhanced fluid flow and heat transfer analysis over a permeable cylinder, *Int. J. Thermofluids*, **26** (2025), 101129. https://doi.org/10.1016/j.ijft.2025.101129
47. T. Körpinar, Z. Körpinar, A. Akgül, Q. Al-Mdallal, Nonlinear normalized fractional electroosmotic spacelike fluid model, *Int. J. Thermofluids*, **26** (2025), 101057. https://doi.org/10.1016/j.ijft.2025.101057

48. K. A. Abro, I. Q. Memon, A. Yousef, Q. M. Al-Mdallal, A comparative analysis of fractal and fractionalized thermal non-equilibrium model for chaotic convection saturated by porous medium, *S. Afr. J. Chem. Eng.*, **51** (2025), 124–135. https://doi.org/10.1016/j.sajce.2024.10.012
49. Y. C. Shiah, C. L. Tan, Boundary element method for thermoelastic analysis of three-dimensional transversely isotropic solids, *Int. J. Solids Struct.*, **49** (2012), 2924–2933. https://doi.org/10.1016/j.ijsolstr.2012.05.025
50. H. Ding, W. Chen, L. Zhang, *Elasticity of transversely isotropic materials*, Dordrecht: Springer, 2006. https://doi.org/10.1007/1-4020-4034-2
51. R. G. Payton, *Elastic wave propagation in transversely isotropic media*, Dordrecht: Springer, 1983. https://doi.org/10.1007/978-94-009-6866-0
52. A. K. Kheibari, M. Jafari, M. B. Nazari, Propagation of heat wave in composite cylinder using Cattaneo–Vernotte theory, *Int. J. Heat Mass Tran.*, **160** (2020), 120208. https://doi.org/10.1016/j.ijheatmasstransfer.2020.120208
53. A. E. Abouelregal, H. M. Sedighi, Thermoelastic characteristics of moving viscoelastic nanobeams based on the nonlocal couple stress theory and dual-phase lag model, *Phys. Scr.*, **97** (2022), 114003. https://doi.org/10.1088/1402-4896/ac97cc
54. H. Zhou, P. Li, Nonlocal dual-phase-lagging thermoelastic damping in rectangular and circular micro/nanoplate resonators, *Appl. Math. Model.*, **95** (2021), 667–687. https://doi.org/10.1016/j.apm.2021.02.035
55. L. Hai, D. J. Kim, Nonlocal dual-phase-lag thermoelastic damping in small-sized circular cross-sectional ring resonators, *Mech. Adv. Mater. Struct.*, **31** (2024), 7498–7514. https://doi.org/10.1080/15376494.2023.2245822
56. C. Li, J. Liu, T. He, Nonlocal dual-phase-lag Cattaneo-type thermoelastic diffusion theory and its application in 1D transient dynamic responses analysis for copper-metallic layered structure, *Acta Mech.*, **235** (2024), 6341–6363. https://doi.org/10.1007/s00707-024-04050-6
57. X. Li, X. Tian, The thermal injury analysis of skin tissue with a new nonlocal dual phase lag model, *Waves in Random and Complex Media*, **35** (2025), 6669–6682. https://doi.org/10.1080/17455030.2022.2080299
58. A. E. Abouelregal, M. Marin, Y. Alhassan, D. Atta, A novel space–time nonlocal thermo-viscoelastic model with two-phase lags for analyzing heat diffusion in a half-space subjected to a heat source, *Iran. J. Sci. Technol. Trans. Mech. Eng.*, **49** (2025), 1315–1332. https://doi.org/10.1007/s40997-025-00835-9
59. R. Quintanilla, Moore–Gibson–Thompson thermoelasticity with two temperatures, *Appl. Eng. Sci.*, **1** (2020), 100006. https://doi.org/10.1016/j.apples.2020.100006
60. A. E. Abouelregal, K. Alanazi, Dynamics of a viscoelastic microbeam on Winkler foundation induced by laser excitation: a nonlocal MGT heat conduction approach, *ZAMM-Z. Angew Math. Mech.*, **105** (2025), e70159. https://doi.org/10.1002/zamm.70159
61. A. E. Abouelregal, M. Marin, S. S. Askar, A. Foul, Thermomagnetic transient analysis of an infinitely long transverse isotropic annular cylinder using the MGT fractional heat conduction model with a non-singular kernel, *J. Vib. Eng. Technol.*, **12** (2024), 557–572. https://doi.org/10.1007/s42417-024-01432-x
62. G. Chen, Non-Fourier phonon heat conduction at the microscale and nanoscale, *Nat. Rev. Phys.*, **3** (2021), 555–569. https://doi.org/10.1038/s42254-021-00334-1

63. M. Caputo, M. Fabrizio, A new definition of fractional derivative without singular kernel, *Prog. Fract. Differ. Appl.*, **1** (2015), 73–85.
64. M. Caputo, M. Fabrizio, On the notion of fractional derivative and applications to the hysteresis phenomena, *Meccanica*, **52** (2017), 3043–3052. https://doi.org/10.1007/s11012-017-0652-y
65. L. Bawankar, G. D. Kedar, Initial stress and modified Ohm's law in magneto-thermoelastic problem under three theories with microtemperatures and voids, *Int. J. Thermodyn.*, **25** (2022), 54–63. https://doi.org/10.5541/ijot.934363
66. Y. Jiang, J. Shi, P. Wang, H. Zha, X. Lin, F. Liu, et al., Compact two-stage pulse compression system for producing gigawatt microwave pulses, *IEEE Trans. Microw. Theory Tech.*, **69** (2021), 4533–4540. https://doi.org/10.1109/TMTT.2021.3093554
67. B. Davies, B. Martin, Numerical inversion of the Laplace transform: a survey and comparison of methods, *J. Comput. Phys.*, **33** (1979), 1–32. https://doi.org/10.1016/0021-9991(79)90025-1
68. A. M. Cohen, *Numerical methods for Laplace transform inversion*, New York: Springer, 2007. https://doi.org/10.1007/978-0-387-68855-8
69. A. Kuznetsov, On the convergence of the Gaver–Stehfest algorithm, *SIAM J. Numer. Anal.*, **51** (2013), 2984–2998. https://doi.org/10.1137/13091974X
70. G. Honig, U. Hirdes, A method for the numerical inversion of Laplace transforms, *J. Comput. Appl. Math.*, **10** (1984), 113–132. https://doi.org/10.1016/0377-0427(84)90075-X
71. M. Eroğlu, I. Esen, M. A. Koç, Thermal vibration and buckling analysis of magneto-electro-elastic functionally graded porous higher-order nanobeams using nonlocal strain gradient theory, *Acta Mech.*, **235** (2024), 1175–1211. https://doi.org/10.1007/s00707-023-03793-y
72. M. Malikan, V. A. Eremeyev, On dynamic modeling of piezomagnetic/flexomagnetic microstructures based on Lord–Shulman thermoelastic model, *Arch. Appl. Mech.*, **93** (2023), 181–196. https://doi.org/10.1007/s00419-022-02149-7
73. H. Sharifi, Magneto–thermoelastic behavior of an orthotropic hollow cylinder based on Lord–Shulman and Green–Lindsay theories, *Acta Mech.*, **235** (2024), 4863–4886. https://doi.org/10.1007/s00707-024-03985-0
74. S. Biswas, Eigenvalue approach to a magneto-thermoelastic problem in transversely isotropic hollow cylinder: comparison of three theories, *Waves in Random and Complex Media*, **31** (2021), 403–419. https://doi.org/10.1080/17455030.2019.1588484
75. M. K. Dehkordi, Y. Kiani, Lord–Shulman and Green–Lindsay-based magneto-thermoelasticity of hollow cylinder, *Acta Mech.*, **235** (2024), 51–72. https://doi.org/10.1007/s00707-023-03739-4
76. A. Alansari, Fractional three-phase-lag heat transfer model for analyzing perfect conducting thermelastic hollow cylinder, *Mech. Solids*, **60** (2025), 2858–2873. https://doi.org/10.1134/S0025654425600977
77. P. Xie, T. He, Investigation on the electromagneto-thermoelastic coupling behaviors of a rotating hollow cylinder with memory-dependent derivative, *Mech. Based Des. Struct. Mach.*, **51** (2023), 3119–3137. https://doi.org/10.1080/15397734.2021.1919524
78. A. E. Abouelregal, M. Marin, A. Öchsner, The influence of a non-local Moore–Gibson–Thompson heat transfer model on an underlying thermoelastic material under the model of memory-dependent derivatives, *Continuum Mech. Thermodyn.*, **35** (2023), 545–562. https://doi.org/10.1007/s00161-023-01195-y

79. A. E. Abouelregal, M. Alesemi, Fractional Moore–Gibson–Thompson heat transfer model with nonlocal and nonsingular kernels of a rotating viscoelastic annular cylinder with changeable thermal properties, *PLoS ONE*, **17** (2022), e0269862. https://doi.org/10.1371/journal.pone.0269862
80. H. Wang, T. He, Y. Ma, Investigation on the electro-magneto-thermoviscoelastic response of multilayer rotating hollow cylinder based on two-temperature theory and fractional-order viscoelastic systems, *Mech. Adv. Mater. Struct.*, **32** (2025), 4196–4224. https://doi.org/10.1080/15376494.2024.2401177

AIMS Press

© 2026 the Author(s), licensee AIMS Press. This is an open access article distributed under the terms of the Creative Commons Attribution License (https://creativecommons.org/licenses/by/4.0)